ASSESSMENT OF THE PLANETARY BOUNDARY LAYER OVER THE NORTHEASTERN PACIFIC OCEAN: IMPACT OF DUCTING AND HORIZONTAL INHOMOGENEITY ON GNSS RADIO OCCULTATION MEASUREMENTS

A Dissertation

by

THOMAS E. WINNING JR.

BS, The Ohio State University, 2002
BS, University of Oklahoma, 2009
MS, University of Hawai'i - Mānoa, 2014

Submitted in Partial Fulfillment of the Requirements for the Degree of

DOCTOR OF PHILOSOPHY

in

COASTAL AND MARINE SYSTEMS SCIENCE

Texas A&M University-Corpus Christi
Corpus Christi, Texas

December 2023

ASSESSMENT OF THE PLANETARY BOUNDARY LAYER OVER THE NORTHEASTERN PACIFIC OCEAN: IMPACT OF DUCTING AND HORIZONTAL INHOMOGENEITY ON GNSS RADIO OCCULTATION MEASUREMENTS

A Dissertation

by

THOMAS E WINNING JR

This dissertation meets the standards for scope and quality of
Texas A&M University-Corpus Christi and is hereby approved.

Feiqin Xie, Ph.D.
Chair

Chuntao Liu, Ph.D.
Committee Member

Toshiaki Shinoda, Ph.D.
Committee Member

Michael Starek, Ph.D.
Committee Member

Frank Spaniol, Ed.D.
Graduate Faculty Representative

December 2023

ABSTRACT

In the northeastern Pacific Ocean, strong free tropospheric subsidence and cooler sea surface temperatures due to upwelling result in a distinctive planetary boundary layer (PBL), marked by a sharp temperature inversion and moisture gradient. This distinct subtropical eastern ocean region showcases a unique transition from a shallow stratocumulus-topped PBL near the southern California coast to a deeper trade cumulus PBL regime closer to Hawaii. The shallow PBL coupled with frequent cloudiness poses significant challenges for conventional space-based observations and simulations in weather and climate models. The Global Navigation Satellite System (GNSS) radio occultation (RO) technique excels in sensing the PBL due to its superior vertical resolution, global coverage, and all-weather observation capability. This dissertation is comprised of three major tasks aimed at assessing the potential and limitation of GNSS RO for PBL sensing over the northeastern Pacific Ocean. First, the RO refractivity data from the first Constellation Observing System for Meteorology, Ionosphere, and Climate (COSMIC-I) for the years 2007 to 2012 were used to derive the PBL height (PBLH) climatology over the Northeastern Pacific Ocean. The PBL in this region is characterized by pronounced temperature inversions and moisture gradients across the PBLH, leading to dominant ducting conditions that introduce significant negative biases in RO refractivity retrievals. Consequently, the second task examines the characteristics of the elevated ducting layer along the transect between Los Angeles, California and Honolulu, Hawaii with high-resolution radiosondes from the MAGIC field campaign and ERA5 global reanalysis data. A systematic negative refractivity bias (N-bias) below the ducting layer is observed throughout the transect, peaking approximately 70 meters below the PBL height (−5.42%), and gradually decreasing towards the surface (−0.5%). Third,

the noticeable horizontal inhomogeneity, especially near the PBLH along the transect, may introduce additional RO retrieval errors, warranting further investigation. Using MAGIC radiosonde observations, a 2-dimensional (2D) model of atmospheric refractivity is created which integrates key PBL parameters. An asymmetry index is introduced to measure the extent of horizontal inhomogeneity. Then multiple phase screen (MPS) simulations were carried out to assess the impact of ducting and horizontal inhomogeneity on GNSS RO soundings. Preliminary findings highlight ducting as the primary cause of negative *N*-bias in RO retrieval, while horizontal inhomogeneity within the PBL contributes an additional −1% near the PBL top. This research enhances understanding of RO data quality within the PBL, paving the way for improved RO data assimilation and advancing weather and climate prediction capabilities.

DEDICATION

Words of appreciation are simply not enough to express my gratitude for the two people who were instrumental throughout this process. I dedicate this to my father, Tom and to my best friend, Lindsey. I thank you both for being there when I needed it the most, for sharing the accomplishment and for encouraging me when I was ready to quit. I began with the goal of finishing, and I could not have finished without either of you. Thank you for your love, your support and your belief in me. I love you both.

ACKNOWLEDGEMENTS

I would like to thank Dr. Yi-Leng Chen at the University of Hawai'i – Mānoa for guiding my Master's degree work and for the introduction into radio occultation. I would also like to thank Dr. Feiqin Xie at Texas A&M University – Corpus Christi for the time and effort he allowed for me to invest in this topic on a much deeper level. Additionally, I would like to thank my committee members for their support, timely feedback and helping me though the dissertation process. I would also like to thank my former office partners, Kevin Nelson, Ben Johnston, Isabella Fortunato and Xiao Yu for the support, their help with computer code, brainstorming, healthy academic debate, camaraderie and mindfulness to remember to take time for other pursuits as research allows.

Funding for Section 2: **Estimation of the Marine Boundary Layer Height over the Central North Pacific Using GPS Radio Occultation** was provided by the National Science Foundation award number AGS-1142558 to the University of Hawai'i– Mānoa. This project is also partially supported by NASA grant NNX14AK17G to Texas A&M University – Corpus Christi. COSMIC data were downloaded from the Taiwan Central Weather Bureau (http://tacc.cwb.gov.tw/cdaac/) whereas the NCEP-FNL data were downloaded from the Research Data Archive at the National Center for Atmospheric Research, Computational and Information Systems Laboratory, Boulder, CO [Available online at http://rda.ucar.edu/datasets/ds083.2].

Funding for Section 3: **Assessing the Ducting Phenomenon and its Impact on GNSS Radio Occultation Refractivity Retrievals over the Northeast Pacific Ocean using Radiosondes and Global Reanalysis** and Section 4: **Assessing the Horizontal Inhomogeneity**

in the Lower Troposphere and its Impact on GNSS Radio Occultation Retrievals – a Simulation Study was partially provided from NASA grant (NNX15AQ17G) as well as the graduate research assistantship from the Coastal Marine System Science Program at Texas A&M University – Corpus Christi. The high-resolution ERA5 reanalysis data were acquired from ECMWF. The MAGIC radiosonde data were provided by the Atmospheric Radiation Measurement program (ARM) Climate Research Facility sponsored by the U.S. Department of Energy (DOE).

TABLE OF CONTENTS

Page

ABSTRACT iv

DEDICATION vi

ACKNOWLEDGEMENTS vii

TABLE OF CONTENTS ix

LIST OF FIGURES xii

LIST OF TABLES xv

1. INTRODUCTION 1

1.1 The planetary boundary layer 1

1.1.1 PBLH observation 2

1.1.2 RO refractivity retrieval biases (*N*-biases) due to ducting 3

1.1.3 Assessing the impact of horizontal inhomogeneity on GNSS RO 3

1.2 References 4

2. ESTIMATION OF THE PLANETARY BOUNDARY LAYER HEIGHT OVER THE CENTRAL NORTH PACIFIC USING GPS RADIO OCCULTATION 6

2.1 Introduction 6

2.2 Seasonal climatology 9

2.2.1 Sea level pressure and surface wind 10

2.3 Data and methods 12

2.3.1 NCEP FNL data 12

2.3.2 COSMIC GPS radio occultation soundings 14

2.3.3 Detecting the inversion base height from GPS RO using the gradient method 15

2.3.4 Relative minimum gradient.. 18

2.4 Results.. 19

2.4.1 Seasonal climatology of PBL height.. 19

2.4.2 PBLH climatology during JJA under trade wind conditions 21

2.4.3 PBLH climatology during DJF under trade wind conditions 22

2.5 Conclusion 25

2.6 References... 27

3. ASSESSING THE DUCTING PHENOMENON AND ITS POTENTIAL IMPACT ON GNSS RADIO OCCULTATION REFRACTIVITY RETRIEVALS OVER THE NORTHEAST PACIFIC OCEAN USING RADIOSONDES AND GLOBAL REANALYSIS 33

3.1 Introduction... 33

3.2 Data and methods 36

3.2.1 MAGIC radiosonde and colocated ERA5 data sets.................................... 36

3.2.2 PBL height detection with the minimum gradient method......................... 37

3.2.3 Ducting layers 39

3.2.4 Evaluation of GNSS RO *N*-bias resulting from ducting............................. 40

3.3 Analysis... 42

3.3.1 PBL analysis 43

3.3.2 Ducting characteristics.. 45

3.3.3 Ducting-induced GNSS RO *N*-bias statistics.. 48

3.3.4 Zonal variation of the *N*-bias along the transect 50

3.3.5 The *N*-bias and key variable relationship 54

3.4 Summary and conclusions 56

3.5 References 58

4. ASSESSING THE HORIZONTAL INHOMOGENEITY IN THE LOWER TROPOSPHERE AND ITS IMPACT ON GNSS RADIO OCCULTATION RETRIEVALS –A SIMULATION STUDY 66

4.1 Introduction 66

4.2 An atmospheric model derived from radiosonde observations 67

4.2.1 A simple 5-segment refractivity model 68

4.2.2 The 2D atmospheric refractivity model 70

4.2.3 Horizontal inhomogeneity and the asymmetry index 72

4.3 Simulation study on the 2D atmospheric model 76

4.3.1 Assessment of ducting induced *N*-bias 78

4.3.2 Multiple phase screen (MPS) simulation of the 2D atmosphere 80

4.3.3 Assessment of the impact of horizontal inhomogeneity on RO refractivity retrievals 81

4.4 Conclusion 83

4.5 References 84

5. SUMMARY AND CONCLUSION 89

5.1 Summary 89

5.2 Conclusion 91

5.3 References 91

APPENDIX: THE 5-SEGMENT REFRACITIVY MODEL 94

LIST OF FIGURES

Page

Figure 2.1. Map of central North Pacific Ocean with the locations of Lihue and Hilo shown. ... 10

Figure 2.2. Seasonal mean climatology of (top row) mean sea level pressure (MSLP in hPa) and (bottom row) surface wind vectors for JJA (left) and DJF (right) with isotachs in 2.5 m s^{-1} increments (2007-2012) from NCEP-FNL Analysis. 12

Figure 2.3 Examples of MSLP (hPa) and surface wind vectors (2.5 m s^{-1} increments) during trade wind (left column) and non-trade wind (right column) days from NCEP-FNL. 14

Figure 2.4. Six year mean COSMIC RO sounding numbers per 5˚ x 5˚ grid in four seasons: DJF, MAM, JJA and SON. 17

Figure 2.5. Six year mean COSMIC RO sounding numbers per 5˚ x 5˚ grid under trade wind conditions for JJA-TW and DJF-TW. 18

Figure 2.6. Six year (5˚ x 5˚ grid) median value of the estimated seasonal PBL height (km) for DJF, MAM, JJA, and SON. 23

Figure 2.7. Standard deviation of PBL height (km) over the region for DJF, MAM, JJA, and SON. 23

Figure 2.8. Horizontal distribution of inversion strength, estimated by the RMG for DJF, MAM, JJA, and SON. 24

Figure 2.9. Six year median value of the PBLH (km, top), standard deviation of PBL height (km, middle), and RMG (bottom) under trade wind conditions for JJA-TW (left) and DJF-TW (right). 25

Figure 3.1. Location of radiosonde observations from the MAGIC field campaign October 2012–September 2013 37

Figure 3.2. Vertical profiles of refractivity (1/10 x N in N-units, N/10, solid blue), temperature (T in ˚C, dotted red) and specific humidity (q in g kg−1, dashed green) for (a) radiosonde at (23.69˚N, -150.02˚E) launched at 2012-10-02, 05:30 UTC. 40

Figure 3.3. End-to-end simulation data for MAGIC radiosonde launched at 0530 UTC on 20121002.. 42

Figure 3.4. Zonal transect of 5˚ bin MAGIC and ERA5 PBLH (a), minimum refractivity gradient (b) and sharpness parameter (c) for MAGIC. 44

Figure 3.5. Zonal transect of 5˚ bin median (a) ducting height, (b) ducting layer thickness (Δh), (c) ducting layer strength (ΔN), and (d) average ducting layer gradient $\Delta N/\Delta h$ for MAGIC. 47

Figure 3.6. Comparison of individual profiles' ducting strength (ΔN) vs. ducting thickness (Δh) for MAGIC (a) and ERA5 (b)... 48

Figure 3.7. Fractional refractivity difference (N-bias in %) between the simulated Abel-retrieved refractivity profile and the original observation profile ($(N_{Abel} - N_{Obs})/N_{Obs}$)............................. 50

Figure 3.8. Median N-bias (solid) ± MAD (dotted) along the north Pacific transect for MAGIC radiosondes (a) and ERA5 (b)... 52

Figure 3.9. Zonal transect of 5˚ bin (a) peak N-bias, (b) median PBL N-bias (0.3 km to PBLH), and (c) near surface N-bias at 0.3 km for MAGIC. 54

Figure 3.10. PBLH vs. height of maximum N-bias for individual profiles from MAGIC (a) and ERA5 (b) data. 55

Figure 3.11. (a, b) Minimum refractivity gradient (N-units km^{-1}) and (c, d) sharpness parameter, as a function of the peak N-bias (%). 56

Figure 4.1. Schematic profile of the 5-segment N-model from surface to 10 km. 70

Figure 4.2. (a-d) the median ± median absolute deviation (MAD) of each key parameter of the 5-segment model at 5˚ longitude bin. 71

Figure 4.3. The 2-dimensional refractivity field along the transect from surface to 10 km. 72

Figure 4.4. Asymmetry index profile at MPT −140˚ with horizonal longitude range set as 1˚ (e.g., MPT ± 0.5˚). 74

Figure 4.5. Asymmetry index contour of the 2D atmosphere from 0.5 to 3.5 km, overlaid with the PBLH (white dashed line). 75

Figure 4.6. Linear regression of 2˚ bin PBLH slope (m/km) vs. PBLH. Open circle colors reference the location (longitude) of observations used to calculate the asymmetry index. 76

Figure 4.7. (a) Surface to 5 km comparison of N_m(-140˚) and average profile of $\boldsymbol{Nm}$(−140˚±0.5˚) and (b) fractional difference (($\boldsymbol{Nm}$(−140˚±0.5˚)−- N_m(−140.0˚))/ N_m(−140.0˚)) (solid red) with 1˚ asymmetry at −140˚ (dashed purple) and 1˚ asymmetry (dashed blue). 77

Figure 4.8. (a) The model profile N_m at -140˚ (solid red) and N_{Abel} (dashed blue). 80

Figure 4.9. Comparison of (2D,1D) fractional difference (N_{2D}-N_{1D}/N_{1D}) (negative profiles) and asymmetry (positive profiles) from surface to 5 km at −134˚ (solid purple), −140˚ (dashed blue) and −146˚ (dot dash red). 83

LIST OF TABLES

Page

Table 2.1. Summary of constraints for inclusion of GPS RO vertical profile. 15

Table 3.1. Median and MAD peak N-bias values for MAGIC radiosondes (RDS) and ERA5 for each 5˚ bin. 52

1. INTRODUCTION

1.1 The planetary boundary layer

The planetary boundary layer (PBL) is the lowest layer of the atmosphere that is directly influenced by the surface of the earth (Stull 1988). The shallow PBL coupled with frequent cloudiness poses significant challenges for conventional satellite observations (e.g., passive microwave and infrared sounders) and simulations in weather and climate models. In the past, high vertical resolution PBL observations have largely relied on in-situ methods like radiosonde or lidar with limited spatial and temporal sampling. On the other hand, the Global Navigation Satellite System (GNSS) radio occultation (RO) technique excels in sensing the PBL due to its superior vertical resolution, global coverage, and all-weather observation capability. Global observation is vital for enhancing understanding of the physical processes within the PBL and refining their model representation. The vertical moisture gradients across the temperature inversion that are often observed at the top of the PBL results in a pronounced refractivity gradient which can be precisely detected by GNSS RO observations (Ao et al., 2012, Xie et al., 2012; Basha and Rantam, 2009).

In the northeastern Pacific Ocean, strong free tropospheric subsidence and cooler sea surface temperatures due to ocean upwelling result in a distinctive PBL that is marked by a sharp temperature inversion and moisture gradient. It showcases a unique transition from a shallow stratocumulus-topped PBL near the southern California coast to a deeper trade cumulus-topped PBL closer to Hawaii. The pronounced temperature inversions and vertical moisture gradients across the PBL, lead to dominant ducting conditions (also referred to as super-refraction, SR), which introduce significant negative biases in RO refractivity retrievals (Xie et al., 2012; Ao, 2007; Xie et al., 2006; Sokolovskiy, 2003). On the other hand, the noticeable horizontal inhomogeneity (HI) along the transect, especially near the top of the PBL, may introduce additional errors in the RO refractivity retrievals, as the retrieval process assumes a local spherically symmetric atmosphere (Zeng, 2016). Local spherical symmetry (LSS) is used to ensure that the ray path remains in the occultation plane, which is subject to both along-track and perpendicular horizontal gradients. The former refers to departures caused by gradients within the occultation plane which results in the impact parameter (*a*) not remaining constant over the ray path (Healy, 2001). The along path gradients which occur due to the sharp moisture decreases often seen in the lower troposphere, can lead to a breakdown of the LSS assumption.

This dissertation is comprised of three major tasks aimed at assessing the potential and limitation of GNSS RO for sensing of the PBL over the northeastern Pacific Ocean. First, the RO refractivity data from the first Constellation Observing System for Meteorology, Ionosphere, and Climate (COSMIC-I) for the years 2007 to 2012 were used to derive the PBL height (PBLH) climatology. The second task examines the characteristics of the elevated ducting layer along the transect between Los Angeles, California and Honolulu, Hawaii with high-resolution radiosondes from the MAGIC field campaign and ERA5 global reanalysis data. Third, multiple phase screen (MPS) simulation studies were carried out to assess the impact of horizontal inhomogeneity, especially near the PBLH along the transect, on GNSS RO retrievals.

1.1.1 PBLH observation

In the first task, using the data collected by COSMIC GPS RO, an analysis focusing on seasonal spatial variations of PBL height and strength over the Hawaiian region is performed. The climatology is derived from six years of COSMIC RO data and the mean and standard deviation will be calculated for each season. Focus then turns to a comparison between the mean seasonal climatology and those under trade wind conditions during summer and winter. The PBL height and strength between seasonal climatology and trade-wind climatology is compared in order to identify seasonal and spatial variations of the PBL over the region. See details in Section 2.

1.1.2 RO refractivity retrieval biases (*N*-biases) due to ducting

In the second task, the prevailing ducting phenomena and their impact on GNSS RO observation are studied. Global reanalysis data (ERA5) are collocated with high resolution radiosondes from the MAGIC field campaign over the Northeast Pacific Ocean transect between Los Angeles, California and Honolulu, Hawaii. The ducting characteristics along with detailed statistics of key PBL variables, such as ducting height, PBLH, minimum refractivity gradient, and gradient sharpness are thoroughly assessed with both datasets. Given the high-resolution radiosondes and global reanalysis data, the ducting-induced *N*-bias in simulated GNSS RO refractivity retrievals are achieved by carrying out a two-step end-to-end simulation. For details of this study, see Section 3.

1.1.3 Assessing the impact of horizontal inhomogeneity on GNSS RO

In order to assess the effects of horizontal inhomogeneity (HI) on GNSS RO measurements, a 2-D model of the atmospheric refractivity is created based on the MAGIC radiosonde observations in the third task. Such model integrates key PBL parameters. An asymmetry index is introduced to measure the extent of horizontal inhomogeneity.

Given a 2-D atmospheric model, the GNSS RO signal propagation can be efficiently simulated using the multi-phase-screen (MPS) method (Wang et al., 2020; Ao et al. 2003; Beyerle et al., 2003; Sokolovskiy, 2001). In this method, the atmosphere is approximated by a series of phase screens between which the signal propagates in vacuum. The simulated RO signals can be further processed to retrieve the RO bending angle and refractivity profile given the assumption of the local spherically symmetric atmosphere. Errors in the simulated RO profile, introduced by the presence of horizontal inhomogeneity, can therefore be quantified by comparing the simulated RO retrieval through both homogeneous and inhomogeneous atmosphere; these results are also compared with a statistically averaged input of the 2D atmospheric model.

1.2 References

Ao, C. O., Meehan T. K., Hajj, G. A., Mannucci, A. J., and Beyerle, G.: Lower Troposphere Refractivity Bias in GPS Occultation Retrievals, *J. Geophys. Res.*, 108, 4577, doi:10.1029/2002JD003216, 2003.

Ao, C. O.: Effect of Ducting on Radio Occultation Measurements: An Assessment Based on High-resolution Radiosonde Soundings, *Radio Sci.*, 42, RS2008, doi.org/10.1029/2006RS003485, 2007.

Ao, C. O., Waliser, D. E., Chan, S. K., Li, J.-L., Tian, B., Xie, F., and Mannucci, A. J.: Planetary boundary layer heights from GPS radio occultation refractivity and humidity profiles, *J. Geophys. Res.*, 117, D16117, doi:10.1029/2012JD017598, 2012.

Basha, G., and Ratnam, M. V.: Identification of atmospheric boundary layer height over a tropical station using high-resolution radiosonde refractivity profiles: Comparison with GPS radio occultation measurements, *J. Geophys. Res.*, 114, doi.org/10.1029/2008jd011692, 2009.

Beyerle, G., Gorbunov, M. E., and Ao, C.O.: Simulation studies of GPS radio occultation measurements, *Radio Sci.*, 38, 1084, doi:10.1029/2002RS002800, 2003.

Healy, S. B.: Radio occultation bending angle and impact parameter errors caused by horizontal refractive index gradients in the troposphere: A simulation study, *J. Geophys. Res.*, 106, D11, 11875–11889, doi:10.1029/2001JD900050, 2001.

Sokolovskiy, S. V.: Modeling and Inverting Radio Occultation Signals in the Moist Troposphere, *Radio Sci.*, 36, 441-458, https://doi.org/10.1029/1999RS002273, 2001.

Sokolovskiy, S. V.: Effect of super refraction on inversions of radio occultation signals in the lower troposphere, *Radio Sci.*, 38 (3), https://doi.org/10.1029/2002RS002728, 2003.

Stull, R. B.: An Introduction to Boundary Layer Meteorology. Kluwer Academic Publishers, 666 pp., ISBN 90-277-2768-6, 1988.

Wang, K.-N., Ao, C.O., and de la Torrre Juarez, M.: GNSS-RO refractivity bias correction under ducting layer using surface-reflection signal, *Remote Sensing*, 12, 35, doi:10.3390/rs12030359, 2020

Xie, F., Syndergaard, S., Kursinski, E. R., and Herman, B.M.: An Approach for Retrieving Marine Boundary Layer Refractivity from GPS Occultation Data in the Presence of Super-refraction, *J. Atmos. Oceanic Technol.*, 23, 1629−1644, https://doi.org/10.1175/JTECH1996.1, 2006.

Xie, F., Wu, D. L., Ao, C. O., Mannucci, A. J., and Kursinski, E. R.: Advances and limitations of atmospheric boundary layer observations with GPS occultation over southeast Pacific Ocean, *Atmos. Chem. Phys.*, 12, 903−918, doi:10.5194/acp-12-903-2012, 2012.

Zeng, Z., Sokilovskiy, S., Schreiner, W., Hunt, D., Lin,.J., and Kuo, Y.-H.: Ionospheric correction of GPS radio occultation data in the troposphere, *Atmos. Meas. Tech.*, 9, 335-346, 2016.

2. ESTIMATION OF THE PLANETARY BOUNDARY LAYER HEIGHT OVER THE CENTRAL NORTH PACIFIC USING GPS RADIO OCCULTATION

2.1 Introduction

The northeasterly surface flow over the central North Pacific Ocean is a manifestation of the North Pacific sub-Tropical High (NPSTH). The resulting low level flow, referred to as the trade winds (TW), represent the world's most consistent surface wind field (Malkus, 1956). Along its trajectory, subsiding air from upper levels comes into contact with convectively driven maritime air ascending from the surface. The transition layer between the two represents the interface between the planetary boundary layer (PBL) and the subsiding warm and dry air aloft (Riehl, 1979). The air within PBL is characterized as moist, conditionally unstable, and frequently populated with trade wind cumuli. The subsidence warming in the inversion layer is balanced by radiative cooling and evaporation from the tops of trade cumuli (Betts and Ridgway, 1989; Albrecht et al., 1979; Riehl 1979). The transition layer is marked by a dramatic decrease in water vapor with respect to height and sometimes accompanied by an increase in temperature, which is referred to as the trade wind inversion (TWI). The height of the inversion base varies from about 500 m at the eastern extreme of the subtropical high to about 2 km at the western and equatorial extremities (Malkus and Riehl, 1964; Neiburger et al., 1961). The thickness of the transition layer can vary widely from a few tens of meters to almost 1 km (Bingaman, 2005). The influence of the PBL is expansive and is an instrumental component of stability and the vertical extent of the convective process, vertical heat and moisture fluxes, large-scale circulations, and energy transports (Trenberth and Stepaniak, 2003).

Over the Hawaiian Islands, the trade wind flow and TWI have significant impacts on island-scale airflow as well as local weather and climate. For islands with tops above the inversion, the TWI base serves as a lid forcing the incoming low-level trade wind flow to be deflected on the windward side (Leopold, 1949). Using model sensitivity tests Chen and Feng (2001) proved that airflow around the island is affected by the TWI and not by the upstream Froude number ($Fr = U/Nh$, where U is the cross mountain wind speed, N is stability, and h is the mountain height) alone (Rasmussen et al., 1989; Smolarkiewicz et al., 1988). For mountains with tops or ridges above the base of the TWI, areas of maximum rainfall correspond to regions of persistent orographic lifting of moisture-laden northeast trade winds up the windward slopes. Conversely, areas of low rainfall are found in the leeward areas and atop the highest mountains (Giambelluca et al., 2013) and result in a semi-arid local climate (Chen and Nash, 1994; Chen and Wang, 1994; Giambelluca and Nullet, 1991). For islands with mountaintops or ridges below the TWI base, a rainfall maximum occurs at the summits (Giambelluca et al., 2013; Nguyen et al., 2010).

The height and strength of the TWI vary on a daily basis (Chen and Feng, 1995; Neiburger et al., 1961). The presence of the TWI limits the vertical extent of convective processes like cloud development. The short term variations of the TWI affect the day to day local weather over the Hawaiian Islands. Chen and Feng (1995) examined rainfall patterns over the Island of Hawaii (Big Island) under high and low trade wind inversions during the Hawaiian Rainband Project (HaRP). Their results suggest that for the low- (high-) inversion days, the median daily rainfall on the windward side of the Big Island is about one-half (more than twice) of the HaRP median daily rainfall. On high inversion days, the afternoon orographically induced clouds and showers extend closer to the summits than during low inversion days because the afternoon upslope flow can bring the low-level moist air to higher elevations. Chen and Feng (2001) simulated island airflow and weather for the Big Island under summer trade wind conditions. They showed that the TWI height represents the depth of the moist layer that affects cloud development and convective feedback to the island airflow. For islands with tops below the trade wind inversion, the daily rainfall amounts on the windward side and the mountaintops are higher when the inversion is higher (Hartley and Chen, 2010).

Despite its significant impacts on local weather and climate, except two sounding sites (Hilo and Lihue) (Fig. 2.1), information on the trade wind inversion over the central North Pacific is limited. Soundings from these two stations are strongly affected by the terrain and local winds and may not be representative of the open ocean conditions. Throughout the year, radiosonde analysis reveals the PBL height on the windward side of the southeastern island of Hawaii (Fig. 2.1) is more than 200 m higher than at Lihue, which is located on the windward side of the northwestern island of Kauai (Cao et al., 2007; Bingaman, 2005; Tran, 1995). However, because the Island of Hawaii has massive volcanic cones with heights exceeding 4 km, the differences in PBL height between Hilo and Lihue may not represent the actual spatial variations over the region (Garrett, 1980). Over the open ocean, the satellite derived temperature and moisture profiles do not have adequate resolution to depict the TWI layer. The launch of the first Constellation Observing System for Meteorology, Ionosphere, and Climate (COSMIC) in 2006, allows for atmospheric profiling with 100 m vertical resolution to be extended over the open ocean using the GPS radio occultation (GPS RO) technique (Kursinski et al., 2000).

Previous research demonstrated the effectiveness of using the refractivity gradient method to detect the boundary layer height (PBLH) in the presence of a moisture gradient and temperature inversion (e.g., Basha and Rantam, 2009; Guo et al., 2011; Ao et al., 2012; Xie et al., 2012; Ho et al., 2015). Additionally, Zhou and Chen (2014) assimilated the high vertical resolution GPS RO data from COSMIC satellites into the initial conditions of the Weather

Research and Forecasting (WRF) model. They showed that the TWI is better predicted for a summer trade wind case when GPS RO data is assimilated into the regional WRF models. Additionally, for a winter cold front case, the propagation of the cold front, prefrontal moisture tongue, and postfrontal inversion are better predicted in the high resolution regional domain over the Hawaiian Islands.

Using the data collected by COSMIC GPS RO, an analysis focusing on seasonal spatial variations of PBL height and strength over the Hawaiian region will be performed. Focus will then turn to a comparison between the mean seasonal climatology and those under trade wind conditions during summer and winter. The structure of the chapter is as follows. In Section 2.2, the multi-year mean seasonal climatology of trade wind and non-trade wind conditions are presented. The data and methodology used for the study are described in Section 2.3. Section 2.4 presents the seasonal PBL height climatology as well as the climatology during trade wind only conditions; both derived from COSMIC RO observations. Results during trade wind conditions are then compared with the seasonal PBLH climatology. Our analyses of the PBL heights over the open ocean will also be compared with those at the two Hawaii sounding sites. Finally, Section 2.5 contains the summary and conclusion.

2.2 Seasonal climatology

Throughout the summer months of June, July, and August (JJA) the northeasterly surface flow is present approximately 90% of the time (Schroeder, 1993). Conversely, during the cool season (November-April) the wind pattern is not as uniform as its summer counterpart (Schroeder and Giambelluca, 1998). The pattern difference can be attributed to the annual migration of the NPSTH and polar jet stream which leave the islands vulnerable to Kona low pressure systems, upper level troughs, and cold fronts (Schroeder, 1993; Kodama and Businger, 1998). As a result, the surface trade wind flow is present less than 50% of the time during the core winter months of December, January, and February (DJF) (Schroeder, 1993). The interaction between the islands and the prevailing weather patterns over the Pacific region add layers of complexity during DJF.

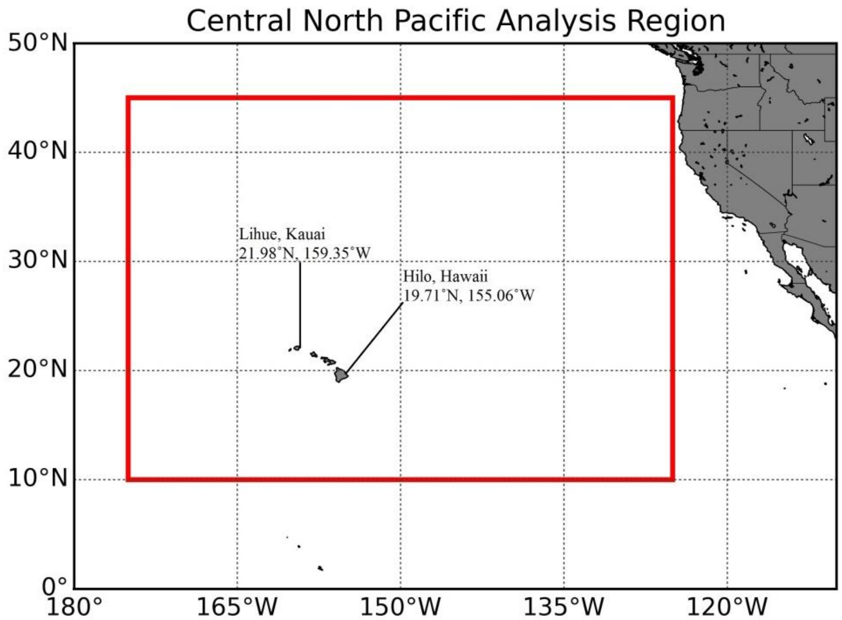

Figure 2.1. Map of central North Pacific Ocean with the locations of Lihue and Hilo shown. The red box denotes the analysis region: 10˚N-45˚N; 125˚W-175˚W.

2.2.1 Sea level pressure and surface wind

The maximum surface pressure associated with the NPSTH during JJA is approximately 1024 hPa and located near 35°N, 150°W as seen in the six year mean (2007-2012) from the National Centers for Environmental Prediction (NCEP) Final (FNL) Operational Global Analysis (Fig. 2.2). During the DJF season, the center of the NPSTH (1022 hPa) is located in the vicinity of 30°N, 130°W, southeast of the JJA position (Fig. 2.2). The location and strength of the NPSTH governs the prevailing surface wind over the central North Pacific region; accordingly, the effects of island interactions vary by season. Climatologically, the surface winds are predominantly from the northeast during JJA with a maximum mean velocity of approximately 7.5 m s^{-1} in an area located south of the Island of Hawaii and bisected by the 15°N latitude line between 150°W and 165°W (Fig. 2.2). Note that while the mean minimum surface wind vectors are seen in the lee of the Hawaiian Islands, the wake circulations (Hafner and Xie, 2003; Yang and Chen, 2003; Smolarkiewicz et al., 1988) are not properly resolved by the NCEP-FNL analysis. As the NPSTH shifts southeastward during DJF, the surface winds upstream of Hawaii shift to a more easterly direction with slightly slower wind speed which moves the area of maximum mean wind speed (7.5 m s^{-1}) to the south side of the Big Island and east to west across the entire analysis domain south of 20°N (Fig. 2.2).

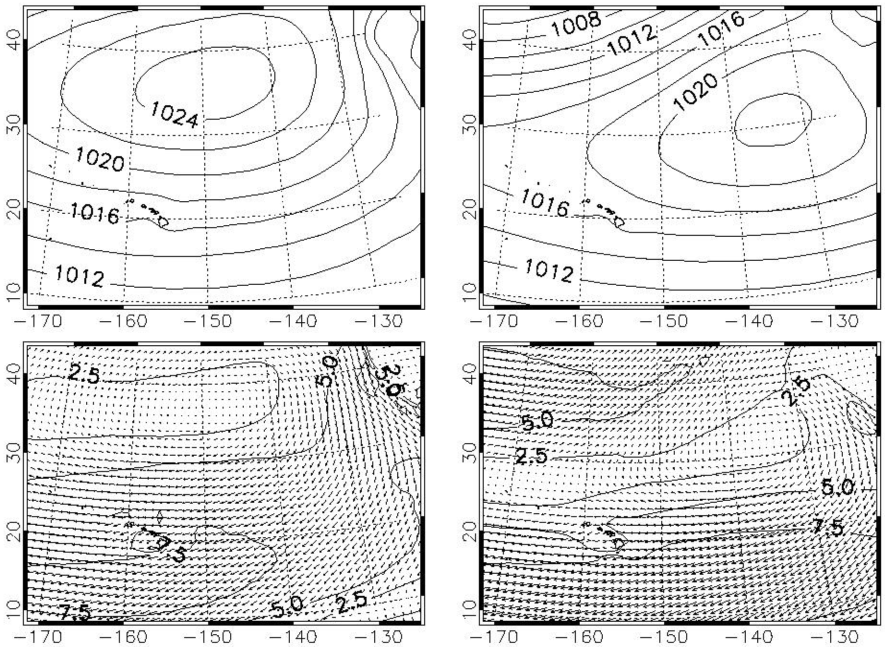

Figure 2.2. Seasonal mean climatology of (top row) mean sea level pressure (MSLP in hPa) and (bottom row) surface wind vectors for JJA (left) and DJF (right) with isotachs in 2.5 m s^{-1} increments (2007-2012) from NCEP-FNL Analysis.

2.3 Data and methods

2.3.1 NCEP FNL data

The difference in PBL height during trade wind and non-trade wind conditions is the primary focus of this study. As such, daily (00 Z and 12 Z) surface maps of mean sea level pressure (MSLP) from the National Center for Environmental Prediction-Final (NCEP FNL) Operational Global Analysis are utilized to identify “trade wind days”. The NCEP FNL data are resolved on a 1˚x1˚ grid with 26 mandatory levels every six hours. The analysis data are obtained from the Computational and Information Systems Laboratory Research Data Archive (http://rda.ucar.edu/datasets/ds083.2). For the purposes of this study, the required synoptic conditions to be considered as “trade wind” flow are defined as surface flow governed by the NPSTH and not influenced by Kona lows, tropical cyclones, cold fronts, or other synoptic disturbances. Therefore, any daily 24-hour period with a disturbance interrupting or enhancing the northeast flow was not considered a trade wind day.

Examples of typical trade wind and non-trade wind surface flow for both JJA and DJF are presented in (Fig. 2.3) from NCEP-FNL. Selected JJA cases are 00Z-24 June 2009 (top left) and 00Z-01 July 2009 (top right). The selected DJF cases are 00Z-04 December 2012 (bottom left) and 00Z-11 December 2008 (bottom right). During trade wind days, northeasterly winds originating from the NPSTH dominate the surface flow across the central North Pacific Ocean. During the non-trade wind days, the synoptic disturbance for both summer and winter seasons led to a decrease or even an absence of NE surface winds. During the six-year period (2007-2012), trade wind days account for 87% of the total observation days during JJA and 47% during DJF.

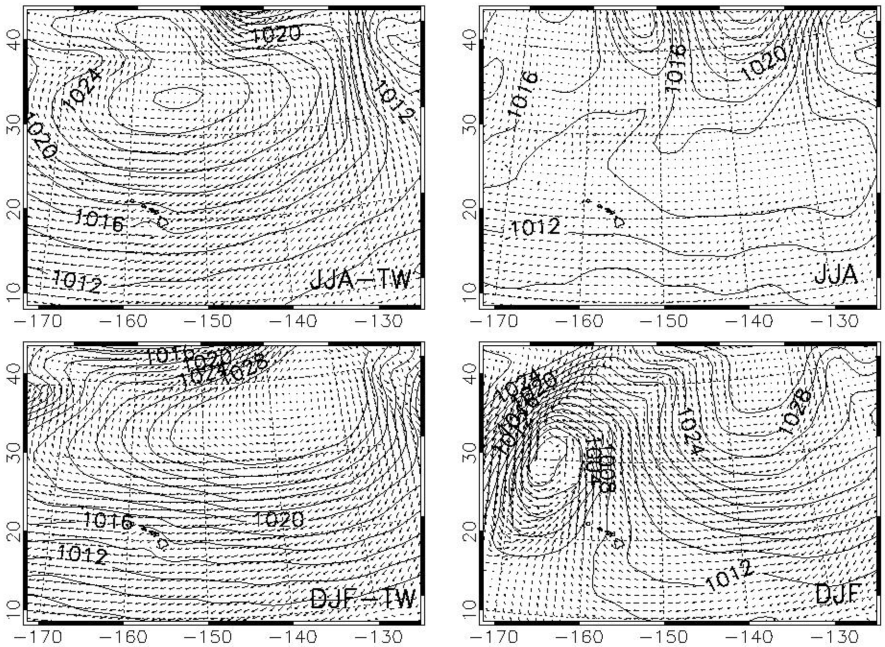

Figure 2.3 Examples of MSLP (hPa) and surface wind vectors (2.5 m s^{-1} increments) during trade wind (left column) and non-trade wind (right column) days from NCEP-FNL.

2.3.2 COSMIC GPS radio occultation soundings

The primary data set used is COSMIC RO refractivity profiles obtained through the Taiwan Analysis Center (http://tacc.cwb.gov.tw/cdaac/). Six years of COSMIC RO profiles over the Hawaiian region from 2007 to 2012 were collected and binned into 5°x5° latitude/longitude grids. Each RO profile was flagged as either trade wind or non-trade wind based on the synoptic condition from the NCEP FNL analysis. The focus is the seasonal climatology of the PBL height for Northern Hemisphere spring (March-April-May, MAM); summer (June-July-August, JJA); fall (September-October-November, SON); and winter (December-January-February, DJF). Additionally, the climatology of the PBL height under trade wind conditions in summer and winter seasons (JJA-TW and DJF-TW) for the years 2007 through 2012 is included in the analysis.

2.3.3 Detecting the inversion base height from GPS RO using the gradient method

The microwave refractivity (N in N-units), in the neutral atmosphere (Smith and Weintraub, 1953) is a function of atmospheric pressure (P in hPa), temperature (T in K), and water vapor partial pressure (P_w in hPa), such that,

$$N = 77.6\frac{P}{T} + 3.73 \times 10^5 \frac{P_w}{T^2}, \tag{2.1}$$

where a_1= 77.6 (K hPa^{-1}) and a_2 = 3.73 x 10^5 (K^2 hPa^{-1}).

The first term on the right-hand-side of equation 2.1 represents the dry term of the refractivity value while the second term accounts for the contribution of moisture (Bean and Dutton, 1966). The vertical refractivity gradient (eq. 2.2) is calculated by differentiating the microwave refractivity equation (eq. 2.1) with respect to height (Ao et al., 2012), where

$$N' = \left(\frac{a_1}{T}\right) P' - [a_1 \left(\frac{P}{T^2}\right) + 2a_2 \left(\frac{P_w}{T^3}\right)]T' + \left(\frac{a_2}{T^2}\right) P_w'. \tag{2.2}$$

In equation 2.2, N', P', T', and P_w' are the vertical gradients of refractivity, pressure, temperature, and water vapor pressure, respectively.

The simple gradient method was used to estimate the PBL height from the RO refractivity profiles, i.e., to identify the height of the minimum refractivity gradient as the PBL height (Ao et al., 2012; Xie et al., 2012). To avoid bias in the PBL height climatology, all RO soundings within the analysis region were quality-controlled before being included for derivation of the climatology (Table 2.1).

Table 2.1. Summary of constraints for inclusion of GPS RO vertical profile.

Bin size	Minimum height	Maximum height	Minimum refractivity gradient
5° x 5°	500 m	3.5 km	< −40 N-units km^{-1}

Any sounding that did not penetrate within 500 m above mean sea level was discarded (Ao et al., 2012; Xie et al., 2012; Guo et al., 2011). The minimum refractivity gradient is identified for each RO sounding between the lowest height (≤ 500 m) and 3.5 km above the surface. Previous studies used a maximum height threshold between 3.5 km and 6.0 km (Ao et al., 2012; Xie et al., 2012; Guo et al., 2011) to account for larger boundary layer height variation, especially over land. For a study region over the open ocean, the maximum height threshold does not affect our results. Moreover, to allow for a more robust PBL detection, the minimum refractivity gradient was required to be less than -40 N-units km^{-1}. When an inversion is present, a sharp moisture gradient exists at the top of the PBL over the analysis region resulting in a minimum refractivity gradient with values that frequently range between -60 and -80 (N-units km^{-1}) (Ao et al., 2012). With the implementation of data constraints, the number of valid RO profiles was reduced by roughly 50% from those that were initially available. All valid RO profiles were used to construct the seasonal PBL height climatology and then the analysis was focused on trade wind only profiles for JJA and DJF, based on the synoptic condition from the NCEP-FNL reanalysis. The zonal distribution of GPS RO observations (Fig. 2.4) shows a rather homogeneous sampling pattern between 10°N and 20°N; variability increases north of the island chain with a maximum located in the area of 30°N between 120°W and 140°W.

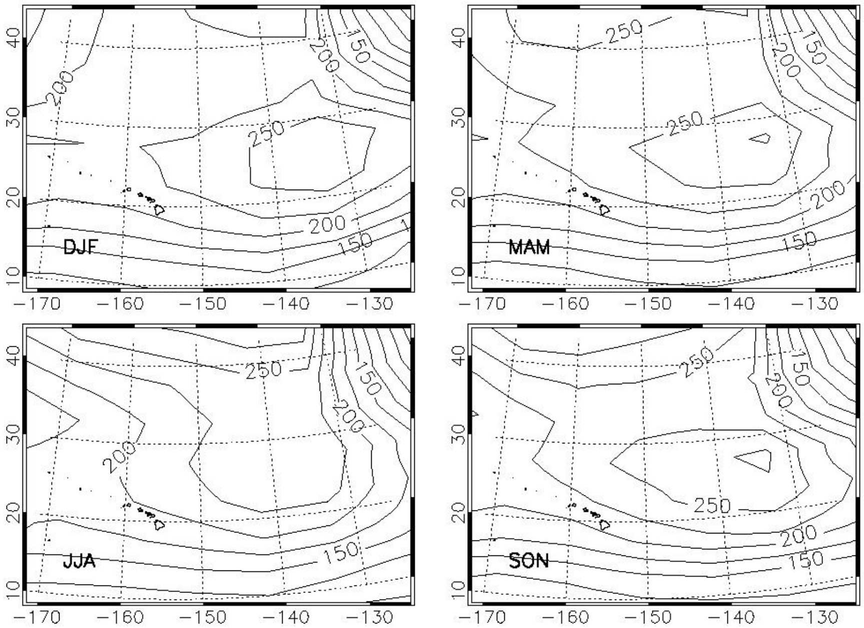

Figure 2.4. Six year mean COSMIC RO sounding numbers per 5° x 5° grid in four seasons: DJF, MAM, JJA and SON.

COSMIC sounding numbers under trade wind conditions (Fig. 2.5) do not vary during JJA-TW due to the large percentage (87%) of trade wind days during the summer season. Conversely, RO soundings under trade wind conditions during DJF-TW reduced by about half as a result of a much smaller percentage (47%) trade wind days due to the closer proximity at which synoptic disturbances pass the islands.

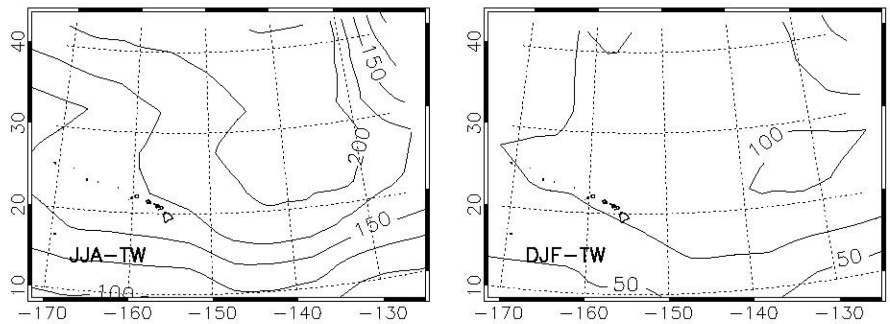

Figure 2.5. Six year mean COSMIC RO sounding numbers per 5˚ x 5˚ grid under trade wind conditions for JJA-TW and DJF-TW.

The simple gradient method was applied to each refractivity profile to calculate the minimum gradient value and associated height at which it occurs. The height of the minimum refractivity gradient ($N' < -40$ N-units km^{-1}) defines the top of the PBL. Note that radiosonde observations indicate that the inversion base height is slightly lower but consistent with the height of the maximum temperature gradient (de Szoeke et al., 2009). In this study, the minimum gradient heights derived from the RO refractivity soundings were used as proxy for the height of the PBL. After all the profiles were binned into 5° x 5° grids in the study region, median and standard deviation values for PBL height climatology were calculated.

2.3.4 Relative minimum gradient

The relative minimum gradient (RMG) is a unitless value that quantifies the magnitude of the minimum refractivity gradient value that is used to identify the top of the PBL (Ao et al., 2012). As seen in equation 2.3, the RMG (N'_{rmg}) is calculated by dividing the minimum refractivity gradient (N'_{min}) by the root mean square (RMS) of the refractivity gradient (N'_{rms}) (Eq. 2.4) over the specified layer of the profile (between 500 m and 3.5 km). The resulting ratio provides a proxy for the strength of the minimum gradient relative to the profile. A RMG value of 1.0 means the minimum gradient is theoretically no different than the gradient values above or below that height. A sharp inversion layer is defined by a RMG value approaching twice the value of the layer mean RMG for this region.

$$N'_{rmg} = -\frac{N'_{min}}{N'_{rms}} \tag{2.3}$$

$$N'_{rms} = \sqrt{\frac{[(N'^2_1) + (N'^2_2) + \cdots + (N'^2_n)]}{n}} \tag{2.4}$$

The typical structure of the trade wind inversion over the central North Pacific region features the strongest subsidence adjacent to the western coast of North America. The strength of the inversion decreases toward the west and south due to the increasing distance from the center of the NPSTH as well as increasing sea surface temperatures. The results show that the inversion strength, represented by the RMG, is strongest adjacent to the California coast and weakens to the west toward the Hawaiian Islands and south toward the intertropical convergence zone (ITCZ).

2.4 Results

2.4.1 Seasonal climatology of PBL height

Figure 2.6 shows the distinct seasonal variation of the PBL height climatology based on six-years (2007-2012) of COSMIC RO refractivity profiles. The climatology in all seasons features an increase of PBL height from a local minimum (< 1 km) near the coast of Southern California, southwestward to a deeper PBL (~2 km) centered near the Hawaiian Islands. The climatology is consistent with the decrease in large-scale, free tropospheric subsidence from a maximum over the cool eastern Pacific near the Southern California coast to the much warmer region around Hawaii (e.g., Riehl, 1979). The winter season (DJF) shows the largest difference when compared to the other seasons featuring a spread of both the centers of minimum and maximum PBL heights to larger regions. When comparing the PBL height during each season, the highest median values are southwest of the island chain during MAM and appear to progress in a northeasterly direction through JJA until the high median value area of 2.0 km is centered directly over the islands during SON. DJF shows a lower PBL median height value of 1.8 km to the south of the Big Island and to the west along the 15°N parallel. The seasonal variation of the median PBL values is consistent with those determined by the Hilo and Lihue soundings, which also show higher heights during the spring and autumn seasons. However, the PBL height climatology determined by the two radiosonde sounding sites (Lihue and Hilo) in Hawaii shows the median PBL height values at Hilo are about 200 m higher than those at Lihue year round (Bingaman, 2005; Neiburger et al., 1961). In contrast, except for DJF during which the axis of the NPSTH is at its southernmost location (Fig. 2.3), the JJA median PBL height values determined by the RO data are higher in the vicinity of Lihue than Hilo. Furthermore, the PBL median values determined by soundings, especially those from Hilo in JJA are higher than those determined by GPS RO data. It is apparent that the PBL heights on the windward side of the islands under trade wind conditions, especially the Hilo soundings, are affected by orographic lifting and will be discussed further in section 2.4.2.

The standard deviation (STDV) of the PBL height in four seasons is shown in Figure 2.7. A minimum STDV value (~0.55 km) is seen over the subtropical latitude band (15°N-35°N) between Hawaii and California (120°W-150°W). In addition, a clear maximum STDV (> 0.7 km) is located west of the islands near (20°N, 165°W) during the JJA and SON seasons.

The RMG is shown in Figure 2.8. The RMG shows the strongest gradient (> 2) near the coast of Southern California, which weakens southwestward with increasing distance from the NPSTH center (Fig. 2.2) and increased convective mixing when approaching the ITCZ. Near Hawaii, the inversion is strongest during the winter months (DJF). The primary reason for the higher RMG value during SON and DJF can be explained by the southward shift of the ridge axis of the NPSTH toward the island chain (Fig. 2.2), which results in stronger subsidence and a lower MBL top. It is worth noting that the minimum STDV of the PBL height over the subtropical band (15°N-30°N, 120°W-150°W), is over the region of highest RMG values.

2.4.2 PBLH climatology during JJA under trade wind conditions

The PBL climatology during JJA under trade wind only conditions (JJA-TW) is also derived based on the six-years of COSMIC RO refractivity profiles (Fig. 2.9). When compared with mean climatology of JJA (Fig. 2.6), the PBL height for JJA-TW over the entire island chain shows similar features; however, the areal coverage of the deep PBL height (> 1.7 km) slightly increases under trade wind conditions (Fig. 2.9). In both the JJA and JJA-TW cases, the high median value of PBL height is located on the leeward side of the islands. West of Kauai (22.5°N, 162.5°W), the PBL height is approximately 2.1 km. It decreases from 2.0 km over Kauai to 1.9 km over the Big Island during JJA-TW, which is slightly lower than the typical inversion height determined by the Hilo soundings in JJA (~2.1 km) (Bingaman, 2005; Tran, 1995; Grindinger, 1992; Neiburger et al., 1961) on the windward coast of the Big Island. It is apparent that the PBL height, as determined by the Hilo soundings, is not representative of the typical value for the Hawaiian Islands due to significant orographic lifting on the windward side of the Big Island. This is likely caused by the presence of Mauna Loa and Mauna Kea, which have peaks well above the 4 km level (Yang and Chen, 2003; Smolarkiewicz et al., 1988).

The STDV of PBL height for JJA shows a minimum value of 0.55 km, which lies within the 15°N-35°N latitude band between the islands and California, and higher values of over 0.7 km located west of 165°W longitude (Fig. 2.7). Under trade wind conditions, the structure is similar; however, an increased area of the minimum STDV of 0.55 km is present (Fig. 2.9).

Thus, under prevailing summer trade wind conditions, smaller variation of the PBL height covers a slightly larger area when compared to the mean climatology.

The bottom row of Figure 2.9 shows similar features of the RMG as the mean climatology shown in Figure 2.8. In other words, the strongest gradient is observed near the Southern California coast and weakens to the south and west toward Hawaii. However, a significant increase in the area with relatively strong gradients (RMG >1.5) under trade wind conditions is revealed.

2.4.3 PBLH climatology during DJF under trade wind conditions

Throughout the DJF season, the mean PBL height climatology is lower under all conditions (Fig. 2.6) compared to trade wind (DJF-TW) conditions (Fig. 2.9). The majority of the island chain has median PBL height values between 1.7 and 1.8 km, with an estimated height over the Big Island between 1.8 and 1.9 km. The highest PBL height (1.9 km) in DJF-TW is centered near (15°N, 150°W) and covers an area much larger than that in the mean climatology. The STDV of PBL height estimates during DJF-TW are generally smaller than the mean climatology (Fig. 2.6) and the area with PBL height STDV of 0.55 km extends westward to cover the entire island chain and southward toward near 15°N (Fig. 2.9) under trade wind conditions. The magnitude of the RMG changes less between DJF and DJF-TW than the summer months (Fig. 2.8 & 2.9). The primary reason for this is the southward shift of the ridge axis as described in Section 2.4.1. Comparison of El Niño vs. non-El Niño PBL heights during DJF (not shown) agree with previous conclusions (Cao et al., 2007; Bingaman, 2005), which observe no appreciable difference between the two data sets. Bingaman (2005) noted that the winter drought in El Niño years (Lyons, 1982) is not related to lower PBL height during those years, rather, it is related to below normal rainfall from winter storms.

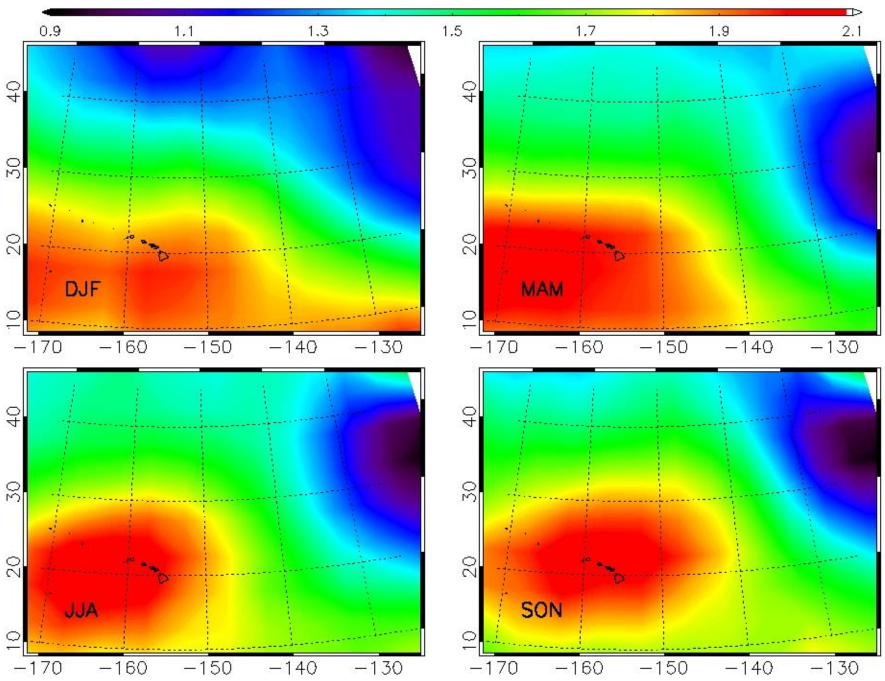

Figure 2.6. Six year (5˚ x 5˚ grid) median value of the estimated seasonal PBL height (km) for DJF, MAM, JJA, and SON.

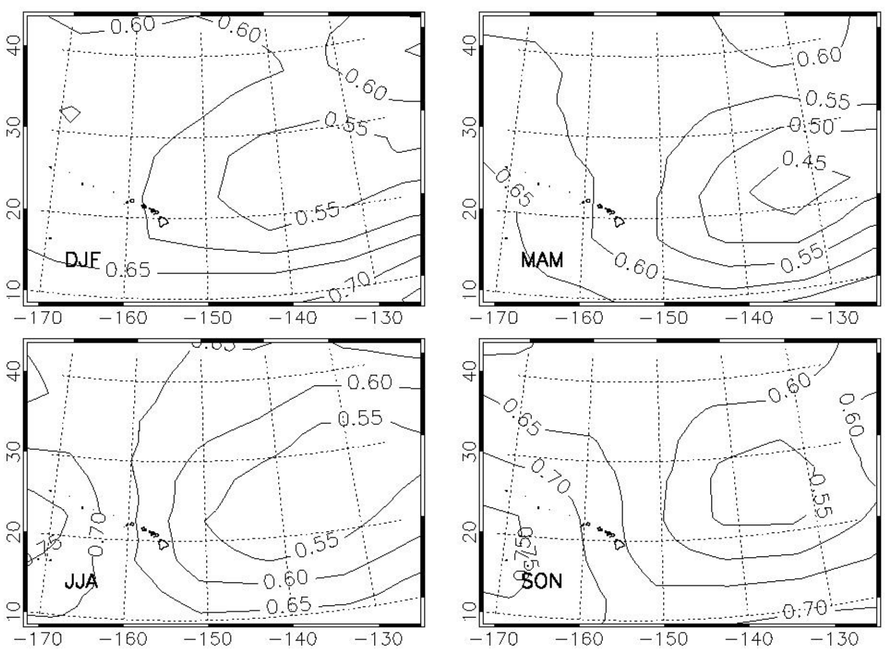

Figure 2.7. Standard deviation of PBL height (km) over the region for DJF, MAM, JJA, and SON.

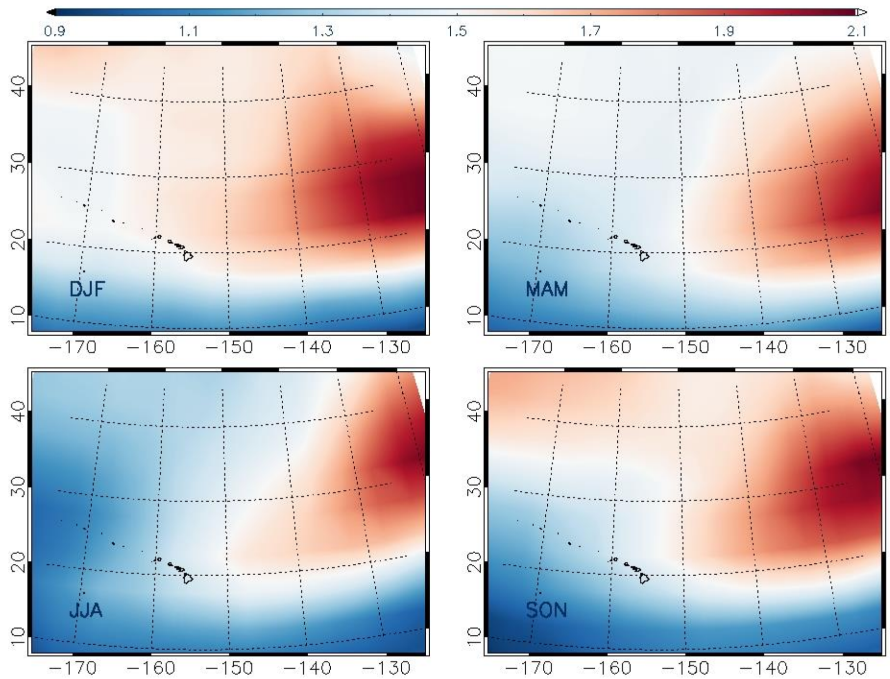

Figure 2.8. Horizontal distribution of inversion strength, estimated by the RMG for DJF, MAM, JJA, and SON.

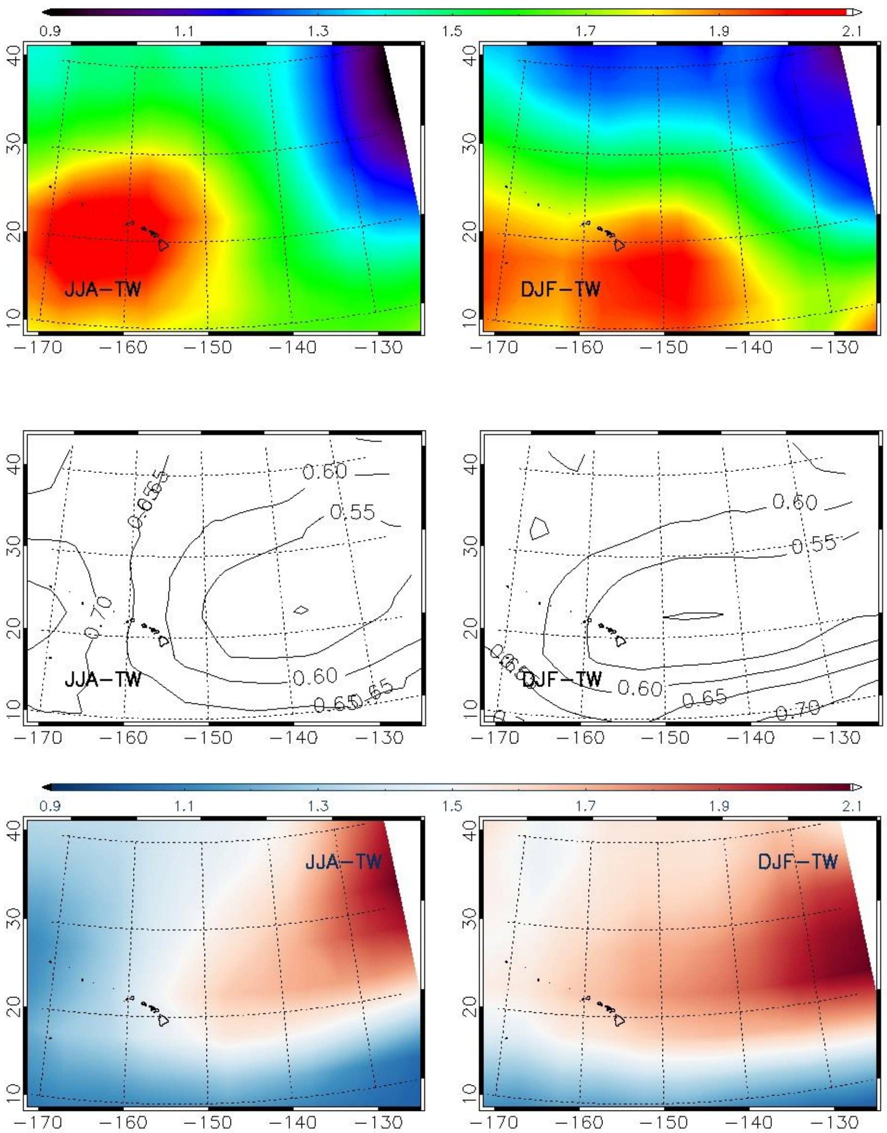

Figure 2.9. Six year median value of the PBLH (km, top), standard deviation of PBL height (km, middle), and RMG (bottom) under trade wind conditions for JJA-TW (left) and DJF-TW (right).

2.5 Conclusion

The island-scale climate and weather under trade wind conditions are not only related to the flow regime (Smolarkiewicz et al., 1988), but also the PBL height with the top identified as the base of TWI (Haratley and Chen 2013; Chen and Feng 1995, 2001; Leopold, 1949). Previous studies of the TWI (strength, height, seasonal variations) over Hawaii utilized rawinsonde data from two sounding sites (Lihue and Hilo), however, soundings taken at both sites are affected by terrain and local winds and may not represent the TWI over the open ocean. Routine observations of the PBL height over the coastal waters of Hawaii are lacking. The COSMIC GPS RO profiles provide the opportunity to study spatial and seasonal variations of the height and strength of the PBL over the central North Pacific for the first time.

In this study our results show that during JJA, when the northeasterly trade winds are prevailing, the median PBL height decreases from 2.0 km over Kauai to 1.9 km over the Big Island with an approximate 2 km maximum that progresses from southwest of the region during MAM to a position directly over the Hawaiian Island chain during SON. If the surface flow is restricted to trade winds only for JJA and DJF, the maximum PBL heights are located over the same areas, but increase to 1.8 km and 2.1 km over the same area during the two respective time periods. The strength of the inversion is stronger when surface winds are restricted to trade wind flow only. In the composite JJA climatology, the RMG is below 2 over the island chain; however, under trade wind conditions the RMG factor over the majority of the islands is between 2.0 and 2.05. The typical PBL height (~ 2.2 km) from previous studies were determined by Hilo soundings (e.g., Schroeder 1993), which were taken on the windward coast of the Island of Hawaii and are probably affected by orographic lifting due to the peaks of Mauna Loa and Mauna Kea, which are well above the 4 km level (Garrett, 1980).

A different spatial pattern of the PBL height occurs during the winter months. During DJF, refractivity profiles reveal a stronger inversion as well as a lower inversion base height in conjunction with the proximity of the NPSTH to the island chain. A high median PBL height of 1.8 km to the southeast of the Big Island increases to 1.9 km when the low level flow is restricted to trade wind flow. In part, this could be due to the seasonal shift of the NPSTH from north of the island chain during JJA to the southeast during DJF. Additionally, trade wind flow occurs only 47% of the time during DJF compared to 87% during JJA. The seasonal variability of PBL height could be the result of seasonal variations in large-scale circulation patterns causing increased variability in surface flow during the winter months. While the RMG factor reflects a value greater than 2.0 over the islands during trade wind conditions, the most noticeable difference occurs during the composite climatology analysis. The RMG factor over the island chain remains at a value of 2.0 or greater for the DJF composite, which is greater than the JJA composite value. The location of the ridge axis and proximity to the island chain during the winter season has resulted in lower PBL heights and stronger magnitude than other seasons. The spatial distribution of the inversion height over Hawaii may be related to the horizontal distribution of large-scale subsidence as well as orographic effects of the island chain (Hafner and Xie, 2003). These issues will be investigated in the future using high resolution numerical models.

2.6 References

Albrecht, B.A., Betts, A.K., Schubert, W.H., and Cox, S.K.: Model of the thermodynamic structure of the trade wind boundary layer: Part I. Theoretical formulation and sensitivity tests, *J. Atmos. Sci.*, 36, 73–89. doi:10.1175/1520-0469(1979)036<0073:MOTTSO>2.0.CO;2. 1979

Ao, C.O., Waliser, D.E., Chan, S.K., Li, J.-L., Tian, B., Xie, F., and Mannucci, A.J.: Planetary boundary layer heights from GPS radio occultation refractivity and humidity profiles, *J. Geophys. Res.*, 117, D16117. doi:10.1029/2012JD017598, 2012.

Basha, G., and Rantam, M.V.: Identification of atmospheric boundary layer height over a tropical station using high-resolution radiosonde profiles: Comparison with GPS radio occultation measurements, *J. Geophys. Res*, 114, D16101. doi:10.1029/2008JD011692, 2009.

Bean, B., and Dutton, E.: Radio Meteorology. Dover Publications, 435 p., 1966.

Betts, A.K., and Ridgway, W.: Climatic equilibrium of the atmospheric convective boundary layer over a tropical ocean, *J. Atmos. Sci.*, 46, 2621–2641. doi:10.1175/1520-0469(1989)046<2621:CEOTAC>2.0.CO;2, 1989.

Bingaman, J.B.: Characteristics of the trade wind inversion over Hawaii. MS Thesis, Dept. of Meteorology, University of Hawaii at Mānoa, Honolulu, HI, 58 p. [Available from Dept. of Atmos. Sci. 2525 Correa Rd., Honolulu, HI 96822.], 2005.

Cao, G., Giambelluca, T.W., Stevens, D.E., and Schroeder, T.A.: Inversion variability in the Hawaiian trade wind regime, *J. Climate*, 20, 1145–1158, 2007.

Chen, Y.-L., and Nash, A.J.: Diurnal variation of surface airflow and rainfall frequencies on the island of Hawaii, *Mon. Wea. Rev.*, 122, 34–56, 1994.

Chen, Y.-L., and Wang, J.-J.: Diurnal variation of surface thermodynamic fields on the island of Hawaii, *Mon. Wea. Rev.*, 122, 2125–2138, 1994.

Chen, Y.-L., and Feng, J.: The influences of inversion height on precipitation and airflow over the Island of Hawaii, *Mon. Wea. Rev.*, 123, 1660–1676. doi: 10.1175/1520-0493(2001)129<1117:NSOAAC>2.0.CO;2, 1995.

Chen, Y.-L., and Feng, J.: Numerical simulations of airflow and cloud distributions over the windward side of the Island of Hawaii. Part I: The effects of trade wind inversion*, *Mon. Wea. Rev.*, 129, 1117–1134. doi:10.1175/1520-0493(2001)129<1117:NSOAAC>2.0.CO;2, 2001.

de Szoeke, S.P., Fairall, C.W., and Pezoa, S.: Ship observations of the tropical Pacific Ocean along the coast of South America, *J. Climate*, 22, 458–464. doi:10.1175/2008JCLI2555.1, 2009.

Garrett, A.J.: Orographic cloud over the eastern slopes of Mauna Loa Volcano, Hawaii, related to insolation and wind, *Mon. Wea. Rev.*, 108 (7), 931–941. doi:10.1175/1520-0493(1980)108<0931:OCOTES>2.0.CO;2, 1980.

Giambelluca, T. W., Chen, Q., Frazier, A. G., Price, J. P., Chen, Y.-L., Chu, P.-S., Eischeid, J. K., and Delparte, D. M.: Online rainfall atlas of Hawai'i, *BAMS*, 94, 313–316, 2013.

Grindinger, C.M.: Temporal variability of the trade wind inversion measured with a boundary layer vertical profiler. M.S. Thesis, Dept. of Meteorology, University of Hawaii at Mānoa. 93 p. [Available from Dept. of Atmos. Sci. 2525 Correa Rd., Honolulu, HI 96822.], 1992.

Guo, P., Kuo, Y.-H., Sokolovskiy, S. V., and Lenschow, D.H.: Estimating atmospheric boundary layer depth using COSMIC radio occultation data, *J. Atmos. Sci.*, 68, 1703–1713. doi:10.1175/2011JAS3612.1, 2011.

Hafner, J., and Xie, S.-P.: Far-field simulation of the Hawaiian wake: Sea surface temperature and orographic effects*, *J. Atmos. Sci.*, 60, 3021–3032. doi:10.1175/1520-0469(2003)060<3021:FSOTHW>2.0.CO;2, 2003.

Hartley, T.M., and Chen, Y.-L.: Characteristics of summer trade wind rainfall over Oahu, *Weather Forecast*, 25, 1797–1815. doi:10.1175/2010WAF2222328.1, 2010.

Ho, S.-P., Peng, L., Anthes, R.A., Kuo, Y.-H., and Lin, H.-C.: Marine boundary layer heights and their longitudinal, diurnal, and interseasonal variability in the southeastern Pacific using COSMIC, CALIOP, and radiosonde data, *J. Climate*, 28, 2856–2872. doi: 10.1175/JCLI-D-14-00238.1, 2015.

Kodama, K.R. and Businger, S.: Weather and forecasting challenges in the Pacific region of the National Weather Service, *Weather Forecast*, 13, 523–546. doi:10.1175/1520-0434(1998)013<0523:WAFCIT>2.0.CO;2, 1998.

Kursinski, E. R., Hajj, G. A., Leroy, S. S. and Herman, B.: The GPS Radio Occultation Technique, *Terr. Atmos. Ocean. Sci. (TAO)*, 11, 53−114, 2000.

Leopold, L.B.: The interaction of trade wind and sea breeze, Hawaii, *J. Meteorol.*, 6, 312–320. doi:10.1175/1520-0469(1949)006<0312:TIOTWA>2.0.CO;2, 1949.

Lyons, S.W.: Empirical orthogonal function analysis of Hawaiian rainfall, *J. Appl. Meteorol.*, 21, 1713–1729, 1982.

Malkus, J.S.: On the maintenance of the trade winds, *Tellus*, 8(3), 335–350. doi: 10.1111/j.2153-3490.1956.tb01231.x, 1956.

Malkus, J. S. and H. Riehl, H.: Cloud Structure and Distributions over the Tropical Pacific Ocean, University of California Press, Berkeley, 229 p., 1964

Neiburger, M., Johnson, D., and Chien, C.: The inversion over the eastern north Pacific Ocean. Studies of the Structure of the Atmosphere over the Eastern Pacific in Summer, Vol. 1, University of California Press, 94 p., 1961.

Nguyen, H.V., Chen Y.-L., and Fujioka, F.: Numerical simulations of island effects on airflow and weather during the summer over the Island of Oahu, *Mon. Wea. Rev.*, 138, 2253–2280, 2010.

Rasmussen, R.M., Smolarkiewicz, P., and Warner, J.: On the dynamics of Hawaiian cloud bands: Comparison of model results with observations and island climatology, *J. Atmos. Sci.*, 46, 1589–1608, 1989

Riehl, H.: Climate and Weather in the Tropics. Academic Press, London, 613 p., 1979.

Schroeder, T.A.: Climate controls. In Sanderson, M. (Ed.), Prevailing Trade Winds: Weather and Climate in Hawaii, University of Hawaii Press, Honolulu, p. 126, 1993.

Schroeder, T.A., and Giambelluca, T., 1998. Climate. In Juvik, S.P., and Juvik, J.O. (Eds.), Atlas of Hawaii, University of Hawaii Press, Honolulu, p. 333, 1998.

Smith, E.K., and Weintraub, S.: The constants in the equation for atmospheric refractive index at radio frequencies, *Proc. IRE*, 41, 39–41. doi:10.1109/JRPROC.1953.274297, 1953.

Smolarkiewicz, P.K., Rasmussen, R.M., and Clark, T.L.: On the dynamics of Hawaiian cloud bands: Island forcing, *J. Atmos. Sci.*, 45, 1872–1905. doi: 10.1175/1520-0469(1988)045<1872:OTDOHC>2.0.CO;2, 1988

Tran, L.T.: Relationship between the inversion and rainfall on the Island of Maui. M.S. Thesis, Dept. of Geography, University of Hawaii at Mānoa, 115 p. [Available from Dept. of Geography. 2424 Maile Way, Honolulu, HI 96822.], 1995.

Trenberth, K.E., and Stepaniak, D.P.: Seamless poleward atmospheric energy transports and implications for the Hadley circulation, *J. Climate*, 16, 3706–3722. doi: 10.1175/1520-0442(2003)016<3706:SPAETA>2.0.CO;2, 2003.

Xie, F., Wu, D.L., Ao, C.O., Mannucci, A.J., and Kursinski, E.R.: Advances and limitations of atmospheric boundary layer observations with GPS occultation over southeast Pacific Ocean, *Atmos. Chem. Phys.*, 12, 903–918. doi:10.5194/acp-12-903-2012, 2012.

Yang, Y., and Chen, Y.-L.: Circulations and rainfall on the lee side of the Island of Hawaii during HaRP*, *Mon. Wea. Rev.*, 131, 2525–2542. doi: 10.1175/1520-0493(2003)131<2525:CAROTL>2.0.CO;2, 2003.

Zhou, C., and Chen, Y.-L.: Assimilation of GPS RO and its impacts on simulations of trade wind inversion and a winter cold front, *Nat. Sci.*, 6, 605–614. http://dx.doi.org/10.4236/ns.2014.68060, 2014.

3. ASSESSING THE DUCTING PHENOMENON AND ITS POTENTIAL IMPACT ON GNSS RADIO OCCULTATION REFRACTIVITY RETRIEVALS OVER THE NORTHEAST PACIFIC OCEAN USING RADIOSONDES AND GLOBAL REANALYSIS

3.1 Introduction

The troposphere, where most weather occurs, consists of two main layers: the planetary boundary layer (PBL) and the free atmosphere (FA) (Garratt, 1994). The PBL characteristics change frequently on both spatial and temporal scales and the PBL height (PBLH) can impact the exchange of heat, momentum, and particulate matter with the FA, making it a critical factor in global energy balances and water cycling (Stull 1988; Ramanathan et al. 1989; Klein and Hartmann 1993). Regular PBL observations are mainly limited to in situ measurements from surface stations and radiosondes. However, spatially and temporally dense in situ PBL observations are only available from field campaigns such as the Boundary Layer Experiment 1996 (BLX96, Stull et al. 1997), the Variability of the American Monsoon Systems (VAMOS) Ocean-Cloud-Atmosphere-Land Study Regional Experiment (VOCALS-REx, Wood et al. 2011), and the Marine Atmospheric Radiation Measurement (ARM) Global Energy and Water Experiment (GEWEX) Cloud System Studies (GCSS) Pacific Cross Section Intercomparison (GPCI) Investigation of Clouds (MAGIC, Zhou et al. 2015). Satellite observations of the PBL are also limited due to signal attenuation of the conventional infrared sounder in the lower troposphere and the low vertical resolution of microwave sounding instruments. Additionally, while the depth of the PBLH can vary from a couple hundred meters to a few kilometers (von Engeln and Teixeira 2013; Ao et al. 2012), the transition layer from the PBL to the FA is typically on the order of tens to hundreds of meters thick (Maddy and Barnet 2008), rendering ineffective PBL sensing from the low vertical resolution passive infrared and microwave sounders.

On the other hand, Global Navigation Satellite System (GNSS) radio occultation (RO) provides global atmospheric soundings with a vertical resolution of approximately 100 m in the lower troposphere under all weather conditions (Gorbunov et al., 2004; Kursinski et al., 2000, 1997). One of the major GNSS RO missions is the Formosat-3/Constellation Observing System for Meteorology, Ionosphere, and Climate (COSMIC), later referred to as COSMIC-1 (Anthes et al. 2008), and its follow-on mission COSMIC-2 (Schreiner et al. 2020). Numerous studies have documented the high value of GNSS RO for profiling the PBL and determining the PBLH (Nelson et al. 2021; Winning et al. 2017; Ho et al. 2015; Ao et al. 2012; ; Guo et al. 2011; Basha and Ratnam 2009; Ao et al. 2008; Xie et al. 2008).

The advancement of the GNSS RO technique with open-loop tracking (Sokolovskiy et al., 2006; Beyerle et al., 2003; Ao et al., 2003) along with the implementation of the radio-holographic retrieval algorithm (Jensen et al., 2004; Jensen et al., 2003; Gorbunov, 2002) have led to much improved PBL sounding quality. However, probing the marine PBL remains challenging as systematic negative biases are frequently seen in RO refractivity retrievals (Feng et al. 2020; Xie et al. 2010). One major cause of the refractivity bias (hereafter *N*-bias) is the RO retrieval error due to elevated atmospheric ducting often seen near the PBLH (Ao et al., 2007; Xie et al., 2006; Ao et al. 2003; Sokolovskiy 2003). This elevated ducting prevails over the subtropical eastern oceans (Feng et al., 2020; Lopez, 2009; von Englen et al., 2003), and the horizontal extent of ducting in these regions can be on the order of thousands of kilometers (Winning et al. 2017; Xie et al. 2010). In the presence of ducting, the vertical refractivity gradient exceeds the critical refraction threshold for L-band frequencies (i.e., $dN/dz \leq -157$ N-units km^{-1}). The steep negative refractivity gradient is often observed in the vicinity of the PBLH, which is typically caused by an atmospheric temperature inversion, a sharp decrease in moisture, or a combination of both. When ducting is present, the Abel inversion (e.g., Fjeldbo et al., 1971) in the standard retrieval process encounters a non-unique inversion problem due to a singularity in the bending angle, resulting in large, systematic underestimation of refractivity (*N*) below the ducting layer (Xie et al. 2006; Ao et al., 2003; Sokolovskiy, 2003). The large uncertainty in RO refractivity coupled with the singularity in bending angle hinders assimilation of RO observations into numerical weather models, resulting in discarding of a significant percentage of RO measurements inside the PBL (Healy, 2001).

To comprehensively assess the potential impact of ducting on GNSS RO retrievals, we begin by constructing a detailed ground truth of PBL ducting statistics. This is derived from an extensive set of high-resolution radiosonde data over the northeastern Pacific Ocean, a region known for prevailing ducting conditions. Subsequently, we conduct a simulation study using the radiosonde data to evaluate the *N*-biases caused by varying ducting characteristics. Section 2 provides details of the two data sets used for this study: high-resolution radiosondes over the northeastern Pacific Ocean and the colocated ECMWF Reanalysis version 5 (ERA5, Hersbach et al. 2020) profiles. Additionally, we discuss the co-location criteria and the detection method for ducting layer and the corresponding PBLH. Section 3 presents the ducting statistics for key variables, such as ducting height, PBLH, minimum refractivity gradient, and sharpness parameter. The characteristics of ducting including the thickness and strength along the cross-section are also shown. Furthermore, we evaluate the ducting-induced *N*-bias in GNSS RO refractivity retrievals by carrying out a two-step end-to-end simulation. Section 4 summarizes the findings and discusses the direction of future research.

3.2 Data and methods

3.2.1 MAGIC radiosonde and colocated ERA5 data sets

A collection of high-resolution radiosondes from the Marine Atmospheric Radiation Measurement (ARM) GCSS Pacific Cross Section Intercomparison (GPCI) Investigation of Clouds (MAGIC) are utilized as the primary data set in this analysis (Lewis 2016; Zhou et al. 2015). The MAGIC field campaign took place from 26 September 2012 to 2 October 2013 as part of the U.S Department of Energy ARM Program Mobile Facility 2 (AMF2) aboard the Horizon Lines container ship, Spirit, which completed 20 round trip passes between Los Angeles, California and Honolulu, Hawaii during the yearlong data collection period (Painemal et al., 2015; Zhou, 2015). During each transit, radiosondes were launched at 6-hour intervals from the beginning of the program through the end of June 2013; the observation frequency increased to every 3 hours from July 2013 through the end of the campaign (Zhou et al., 2015). A total of 583 MAGIC radiosonde profiles were collected during the field campaign (Zhou et al., 2015), all with a vertical sampling frequency of 0.5 Hz (2 seconds), which provides an average vertical resolution of ~8 m below 3 km, but varies due to local vertical motion.

Use of this data set serves multiple benefits. First, the northeast Pacific transitions from a shallow stratocumulus-topped PBL to a higher, trade-cumulus boundary layer regime along the GPCI transect (Garratt, 1994). Second, the large number of observations over a 12-month time frame provides high temporal (diurnal and seasonal) and spatial profiling of the PBL along the GPCI transect seen in Fig. 3.1. Finally, ducting is prevalent throughout the domain which creates a natural cross-section of refractivity field in X (zonal) and Z (vertical) dimensions.

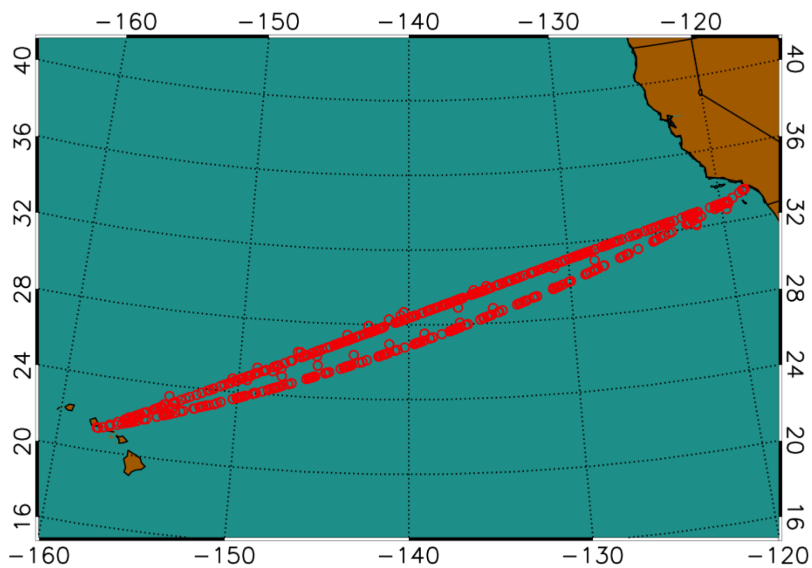

Figure 3.1. Location of radiosonde observations from the MAGIC field campaign October 2012–September 2013

The radiosonde profiles are colocated with ERA5 model reanalysis profiles. The ERA5 reanalysis data have a horizontal grid resolution of 0.25˚x0.25˚, 1-hour temporal resolution, and 137 uneven vertical model levels from the surface to 0.01 hPa. The model level density decreases with height: on average, there are 19 model levels below 1 km (10 –100 m resolution), which reduces to 8 levels between 1 and 2 km (100 – 160 m resolution), and further reduces to 5 levels between 2 and 3 km (160-200 m resolution). Each MAGIC radiosonde profile was colocated with the nearest ERA5 grid point that is within 1.5 hours of the closest 3-hourly model reanalysis profile.

3.2.2 PBL height detection with the minimum gradient method

At GNSS L-band frequencies, the atmospheric refractivity (N in N-units) is derived from the refractive index n, where N = (n − 1) x 106 and, in the neutral atmosphere (Kursinski et al., 1997), is a function of the atmospheric pressure (P in mb), temperature (T in K), and partial pressure of water vapor (Pw in mb) as seen in Eq. (1) from Smith and Weintraub (1953).

$$N = 77.6\frac{P}{T} + 3.73 \times 10^5 \frac{P_w}{T^2}, \quad (1)$$

Over the subtropical eastern oceans, a sharp decrease in moisture is often associated with a strong temperature inversion marking a clear transition from the PBL to the FA. Both the distinct decrease in moisture and the temperature inversion lead to a sharp negative refractivity gradient which can be precisely detected from GNSS RO. Numerous studies have implemented the simple gradient method to detect the PBLH, i.e., the height of the minimum refractivity gradient (Ao et al., 2012; Seidal et al., 2010; Xie et al., 2006). To assess the robustness of PBLH detection with gradient method, Ao et al. (2012) introduced the sharpness parameter (Ñ^') to measure the relative magnitude of the minimum gradient from surface to 5 km as follows:

$$\widetilde{N}' \equiv -\frac{N'_{min}}{N'_{RMS}}, \quad (2)$$

Each refractivity gradient profile can then be filtered to identify the PBLH values with sharpness parameter exceeding a specific threshold, thus increasing the robustness of PBLH detection. In this study, the MAGIC radiosonde refractivity profiles were first interpolated to a uniform 10 m vertical grid and then smoothed by a 100 m boxcar window to reduce the noise in the gradient profile resulting from the high sampling rate. Moreover, the 100 m smoothed radiosonde will be more consistent with the vertical resolution of GNSS RO measurements (e.g. Gorbunov et al., 2004). Colocated ERA5 data were also vertically interpolated to the same 10 m grid but not smoothed as these data do not contain the inherent noise as the radiosonde observations. In addition, as the elevated ducting layer is the focus of this study, the lowest 0.3 km above mean-sea-level of the N-profile near surface are excluded (e.g., Xie et al., 2012). Subsequently, the height of the minimum refractivity gradient (within 0.3 km and 5 km) will be identified as the PBLH.

3.2.3 Ducting layers

When the vertical refractivity gradient is less than the critical refraction (dN/dz ≈ −157.0 N-units km^{-1}), ducting occurs (Sokolovskiy, 2003). A ducting layer is identified as any interval of continuous points with a vertical refractivity gradient equal to or less than −157 N-units km−1. Instances of multiple ducting layers occurring within a profile are present for both the MAGIC (31.5%) and ERA5 (6.7%) data sets. In this study, we only recognize one dominant "ducting layer" in each profile where the minimum vertical gradient is located. The ducting layer thickness (Δh) is defined as the interval between the top and bottom of the ducting layer where the refractivity gradients reach critical refraction. Similarly, the strength of each ducting layer (ΔN) is defined as the refractivity difference between the bottom and top of the ducting layer. The ducting layer height is in reference to the top of the ducting layer (Ao, 2007), which is generally slightly above the PBLH.

Figure 3.2 shows vertical profiles of refractivity (N-units x 1/10, N/10), temperature (T), and specific humidity (q) along with their respective vertical gradients (dN/dz, dT/dz and dq/dz) from a representative MAGIC radiosonde (Fig. 3.2a,b) case located at (23.69˚N, −150.02˚E), and its colocated ERA5 (Fig. 3.2c,d) profile at (23.75˚N, −150.00˚E). The PBLH of the radiosonde (2.10 km) is almost identical to the colocated ERA5 (2.14 km) and the "dominant" ducting layer near the PBLH demonstrates similar thickness. However, a second, weaker ducting layer seen in the radiosonde above the PBLH was not captured by the ERA5.

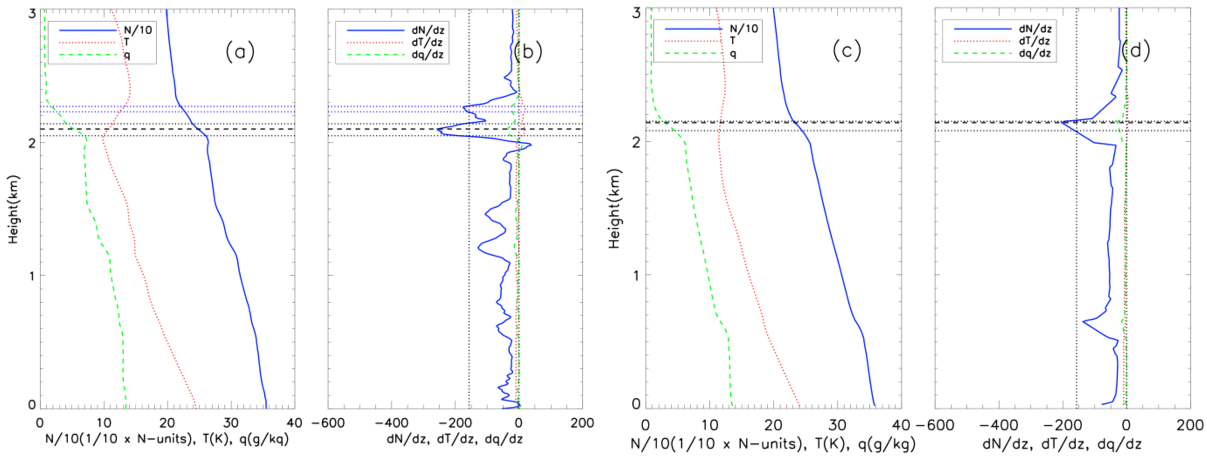

Figure 3.2. Vertical profiles of refractivity (1/10 x N in N-units, N/10, solid blue), temperature (T in ˚C, dotted red) and specific humidity (q in g kg^{-1}, dashed green) for (a) radiosonde at (23.69˚N, -150.02˚E) launched at 2012-10-02, 05:30 UTC, and (c) colocated ERA5 at (23.75˚N, -150.00˚E); and associated gradient profiles for radiosonde (b) and ERA5 (d). The horizontal dashed line highlights the height of the minimum gradient, i.e., PBLH. The paired horizontal dotted lines represent the bottom and top of the two ducting layers in the radiosonde profile (a and b) but only one in the ERA5 profile (c and d).

3.2.4 Evaluation of GNSS RO *N*-bias resulting from ducting

In order to estimate the systematic negative *N*-bias in GNSS RO observations in the presence of ducting, we use an end-to-end simulation on the radiosonde and ERA5 refractivity profiles. The simulation consists of a two-step process adapted from Xie et al. (2006). The first step is to simulate the 1-dimensional GNSS RO bending angle as a function of impact parameter (i.e., the product of refractive index and the radius of the Earth's curvature) by forward Abel integration of an input refractivity profile assuming a spherically symmetric atmosphere (Sokolovskiy, 2001; Eshleman, 1973, Fjeldbo and Eshleman, 1968). The second step is to simulate the GNSS RO refractivity retrieval by applying the Abel inversion on the simulated bending angle from step one. In the absence of ducting, the impact parameter increases monotonically with height, allowing a unique solution to the inverse Abel retrieval that is the same as the original refractivity profile input. However, in the presence of an elevated ducting layer, the Abel retrieval systematically underestimates the refractivity profile due to the non-unique Abel inversion problem resulting from the singularity in bending angle across the ducting layer (Xie et al., 2006; Sokolovskiy 2003). It should be noted that after the 100 m vertical smoothing on radiosonde (no smoothing on ERA5) profiles as described in section 2.2, an additional 50 m vertical smoothing has been applied to the simulated bending angle profiles of both radiosonde and ERA5 data sets to alleviate the challenge of integration through the very sharp bending angle resulting from ducting in the inverse Abel integration procedure (Feng et al., 2020).

Figure 3.3 shows the end-to-end simulation results for the same radiosonde (a–d) and the colocated ERA5 (e–h) cases from Fig. 3.2. Figures 3.3a and 3.33e show refractivity profiles from the radiosonde (N_{rds}) and the colocated ERA5 (N_{ERA5}) data as well as their corresponding Abel refractivity retrievals (N_{Abel}). The PBLH is marked by a horizontal dotted line. The peak bending angle is consistent with the sharp refractivity gradient. Figure 3.3b shows the fractional *N*-bias between the simulated Abel retrieved RO refractivity profile and the observation, i.e., (($N_{Abel} - N_{Obs}$)/N_{Obs}). Considering the significant spatial and temporal variations of ducting height along the transect, each *N*-bias profile is normalized to its PBLH for the purposes of comparison. For example, the zero-adjusted height refers to the PBLH for each individual profile. The systematic negative *N*-bias is clearly shown below the ducting layer marked by the PBLH in both cases, with the biases decreasing at lower altitude, the largest magnitude bias (−5% for radiosonde; −2.5% for ERA5) close to the ducting height and a minimum magnitude approaching zero near the surface.

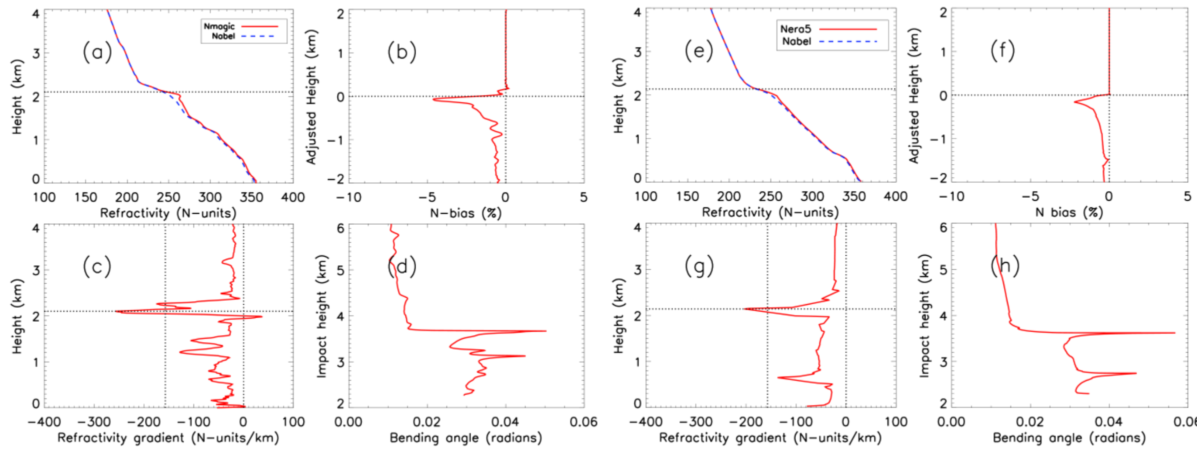

Figure 3.3. End-to-end simulation data for MAGIC radiosonde launched at 0530 UTC on 20121002 showing: (a) N_{Obs} (solid red) and N_{Abel} (blue dashed) from surface to 4 km; (b) PBLH adjusted *N*-bias (($N_{Abel} - N_{Obs}$)/N_{Obs}); (c) refractivity gradient and (d) bending angle vs. impact parameter. The same is shown in panels e-h for the colocated ERA5 profile.

3.3 Analysis

Quality control for radiosonde (and colocated ERA5) profiles was based on five key criteria. First, a total of 19 radiosonde and 24 ERA5 profiles near the southern California coast were removed due to their positions east of −120˚E or anomalously high PBL (PBLH > 3.0 km) with no distinct minimum gradient. The remaining profiles in the easternmost portion of the domain were too few in number to calculate meaningful statistics. Second, any profile lacking critical refraction (i.e. d*N*/dz < −157 N-units km−1) points was excluded from the analysis which resulted in the removal of 47 radiosonde and 176 ERA5 profiles. Third, the noisy bending angle could result in errors in Abel refractivity retrieval and cause positive *N*-bias. Therefore, the profiles with *N*-bias greater than +0.5% are excluded resulting in the removal of 61 MAGIC profiles and 16 ERA5 profiles. Fourth, the profiles with only surface ducting, i.e., below 300 m threshold, are discarded. Finally, 25 radiosonde profiles and 2 ERA5 profiles were removed due to the Abel retrieval failure. After implementing all quality control measures, the number of radiosonde and ERA5 profiles used for the *N*-bias analysis is reduced to 396 and 319 profiles, respectively.

3.3.1 PBL analysis

To evaluate the ducting properties along the transect from the coast of southern California to Hawaii, we group the MAGIC radiosonde and the colocated ERA5 profiles into eight 5˚ longitude bins between −160.0˚ and −120.0˚, which allows for the spatial variation of the PBL, ducting layer and the associated properties along the transect to be easily illustrated. Figure 3.4 shows the median value of PBLH (a), minimum gradient (b) and sharpness parameter (c) along the transect. The median-absolute-deviation (MAD) for each parameter is also shown.

In Fig. 3.4a, the MAGIC radiosondes clearly show the gradual increase of the PBLH along the transect from the shallow stratocumulus-topped PBL (~800 m) near the southern California coast westward to the much deeper trade-cumulus regime (~1.8 km) near Hawaii. A similar structure is seen in the colocated ERA5 data but with an average low bias of 165 m below the radiosonde. However, a nearly 800 m underestimation in PBLH over the two westernmost bins near Hawaii is also seen, this is consistent with what is found over the equivalent trade cumulus region of the subtropical southeast Pacific Ocean (Xie et al., 2012). Such a discrepancy could be due to the sensitivity of gradient method to the vertical resolution of the data. Over the western segment of the transect (near Hawaii), two major gradient layers (one at ~1 km and the other at ~2 km) with comparable refractivity gradients are often observed (e.g., Fig. 3.2). The gradient layer at around 2 km is well-known as the trade-wind inversion. While the lower-level gradient layer at ~1 km, is generally called a mixing layer. Note the radiosonde data exhibit consistent vertical sampling (~8 m resolution) below 3 km, and resolve both layers well. However, the ERA5 data have an uneven vertical sampling intervals increasing with height, with

10 – 100m resolution below 1 km, 100 – 160 m within 1-2 km, and 160 – 200 m within 2-3 km. Therefore, the ERA5 data are more likely to resolve the sharp gradient structure below 1 km than the one at higher altitude. This could result in resolving the mixing layer (below 1 km) with the sharpest refractivity gradient, instead of the trade-wind inversion near 2 km in the ERA5 data. Note that the larger median absolute deviation for the westernmost bins compared to the rest of the transect illustrates the existence of greater PBLH variability closer to the trade-cumulus boundary layer regime. The westward decreasing magnitude of the minimum refractivity gradient (Fig. 3.4b) and sharpness parameter (Fig. 3.4c) indicates the westward weakening of moisture lapse rate and/or temperature inversion across the PBL top, which is consistent with the decreasing synoptic-scale subsidence from the California coast to Hawaii (Riehl, 1979).

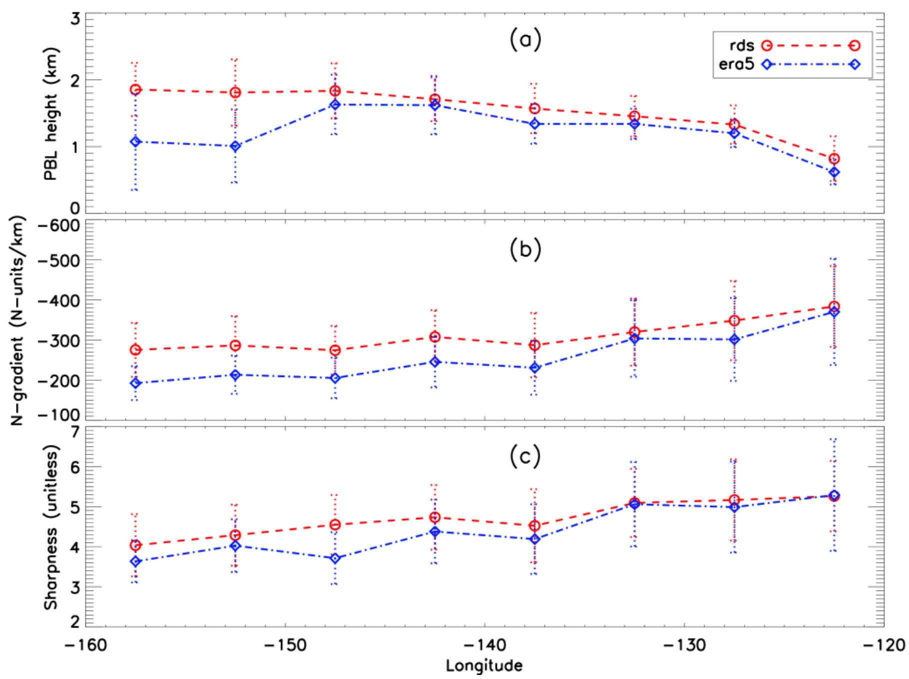

Figure 3.4. Zonal transect of 5° bin MAGIC and ERA5 PBLH (a), minimum refractivity gradient (b) and sharpness parameter (c) for MAGIC (median in red circle and dashed line, MAD in red dotted error bars) and ERA5 (median in blue diamond and dot-dashed line, MAD in blue dotted error bars).

It is also notable that the ERA5 systematically underestimates not only the PBLH but also the magnitude of the minimum gradient across the entire transect. This can also be seen in the sharpness parameter west of −132.5˚. This discrepancy could be partially attributed to the decrease in vertical sampling in ERA5 profiles as compared to the radiosondes, the result of which leads to a weaker PBL refractivity gradient and coincides with an increasing PBLH. Therefore, the underestimation of the ERA5 minimum refractivity gradient increases in magnitude from east to west and becomes most prominent near Hawaii where the PBLH reaches the maximum height over the region.

3.3.2 Ducting characteristics

As introduced in Sect. 3.2.3, the key characteristics of the ducting layer along the transect will be investigated, these include the ducting layer height, thickness (Δh), and strength (ΔN), as well as the average refractivity gradient within the ducting layer (ΔN/Δh). All parameters are interpolated to a 10 m vertical grid.

The ducting layer heights from both radiosonde and ERA5 show a westward increase along the transect is seen in Fig. 3.5a. Note again that the ERA5 shows a systematic ~100–200 m low bias when compared to the radiosondes between −122.5˚ and −147.5˚, with the difference increasing to more than 500 m near Hawaii. The ducting layer thickness is the median height from the bottom of the ducting layer to the top and is expressed in km (Fig. 3.5b). Ducting thickness (Δh) for MAGIC shows a near constant value of 110 m across the entire transect with only a slight increase to 130 m at −122.5˚, consistent with Ao et al. (2003). Conversely, the ERA5 shows a constant but slightly thicker ducting layer to the east of −137.5˚ and then a decreasing thickness to the west of −137.5˚ (Fig. 3.5b).

The ducting layer strength is the decrease in refractivity from the bottom of the ducting layer to the top (Fig. 3.5c) and the ratio $\Delta N/\Delta h$ reflects the average gradient of the ducting layer (Fig. 3.5d). The ducting strength (ΔN) for the radiosondes generally ranges from 25 N-units near Hawaii to 40 N-units near the coast of California. Both ΔN and $\Delta N/\Delta h$ show an overall westward decreasing trend along the transect which is consistent with the decrease in magnitude of the refractivity gradient (Fig. 3.4b). Note that MAGIC and ERA5 show similar ducting strength in the eastern part of the region but diverge near -137.5° with ERA5 10 to 20 N-units weaker than the MAGIC profiles. On the other hand, ERA5 shows a systematic lower average refractivity gradient ($\Delta N/\Delta h$) than MAGIC throughout the transect, indicating the challenge in ERA5 to consistently resolve the sharp vertical structure in refractivity, and likewise in temperature and moisture profiles, across such a thin ducting layer. The problem becomes acutely clear near the trade cumulus region.

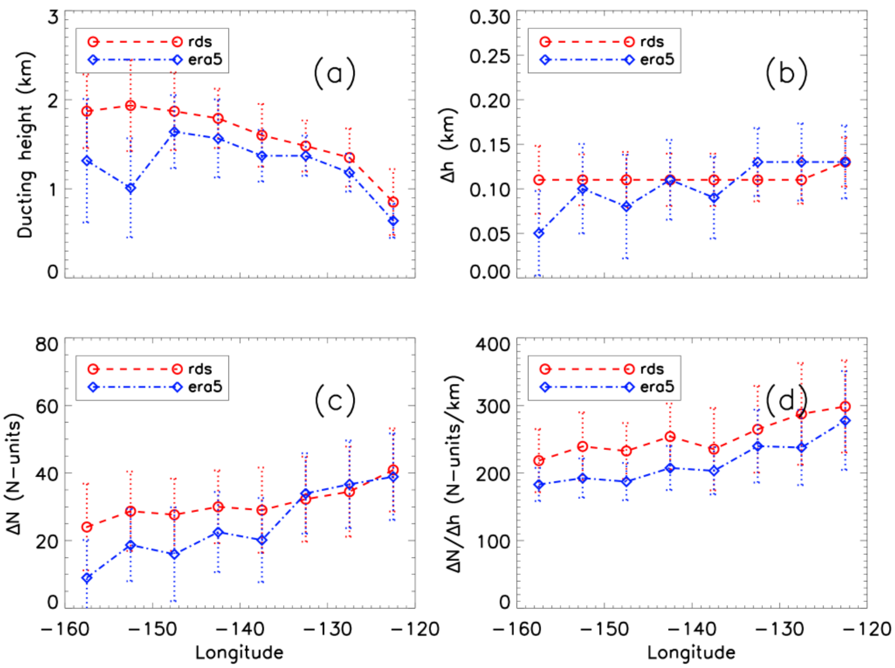

Figure 3.5. Zonal transect of 5° bin median (a) ducting height, (b) ducting layer thickness (Δh), (c) ducting layer strength (ΔN), and (d) average ducting layer gradient $\Delta N/\Delta h$ for MAGIC (median in red circle and red-dashed line, MAD in red-dotted error bars) and ERA5 (median in blue diamond and dot-dashed line, MAD in blue-dotted error bar).

Figure 3.6 shows ducting layer thickness as a function of ducting layer strength, with each data point colored by its respective longitude bin. The relationship between Δh and ΔN is not longitude-dependent for either data set, but a linear trend is evident for thinner ducting layers (Δh < 0.1 km) with weaker ducting strength (ΔN < ~25 N-units). However, for the ducting layers thicker than 0.1 km, such a trend becomes less identifiable, and the ducting strength ΔN begins to show more variability toward larger values.

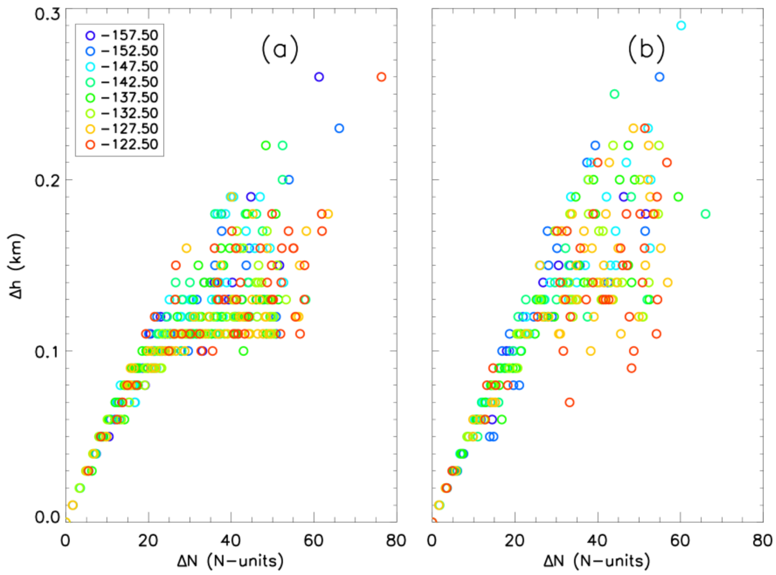

Figure 3.6. Comparison of individual profiles' ducting strength (Δ*N*) vs. ducting thickness (Δ*h*) for MAGIC (a) and ERA5 (b). Circle colors represent the location of the 5° longitude bin of each observation.

3.3.3 Ducting-induced GNSS RO *N*-bias statistics

To estimate the systematic negative *N*-bias in GNSS RO observations due to ducting, we have applied the end-to-end simulation described in sect. 3.2.4 to all radiosonde and ERA5 refractivity profiles with at least one elevated ducting layer detected. The *N*-bias along the transect as well as its relationship to the ducting properties are presented below.

Figure 3.7 shows a composite of both MAGIC (396 profiles) and ERA5 (319 profiles) *N*-bias profiles which have been normalized to their PBLH, with the median *N*-bias and MAD overlaid. The systematic negative *N*-bias peaks at approximately 100 m below the PBLH and decreases at lower altitude. The peak median value of the *N*-bias for radiosondes is −5.42% (MAD, 2.92%), nearly twice the ERA5 value of −2.96% (MAD, 2.59%), indicating the significant underestimation of ducting strength in ERA5 data. However, the variabilities (MAD) of the radiosonde and ERA5 data are within 0.33% of each other, indicating that ERA5 data successfully capture the variations of ducting features seen in the radiosondes. It is worth noting that many radiosonde profiles show small negative *N*-biases above the PBLH (i.e., zero-adjusted height), which is the result of a secondary ducting layer above the major ducting layer near the PBLH. Conversely, few ERA5 profiles show the presence of the secondary ducting layer above PBLH.

A closer look at each data set reveals that the difference between the 5˚ median PBLH and height of the maximum *N*-bias ($h_{PBL} - h_{N\text{-bias}}$) is positive for all bins. The maximum difference of 100 m is located in bin −137.5˚ and a minimum difference of ~15 m at bin −152.5˚. Comparatively, the ERA5 reflects a PBL height greater than the *N*-bias height for each bin with a maximum difference of 230 m located at −142.5˚ and a minimum of ~45 m at −157.5˚. The ERA5 data show a larger average height difference between the PBL and *N*-bias (120 m) than the radiosonde data (80 m).

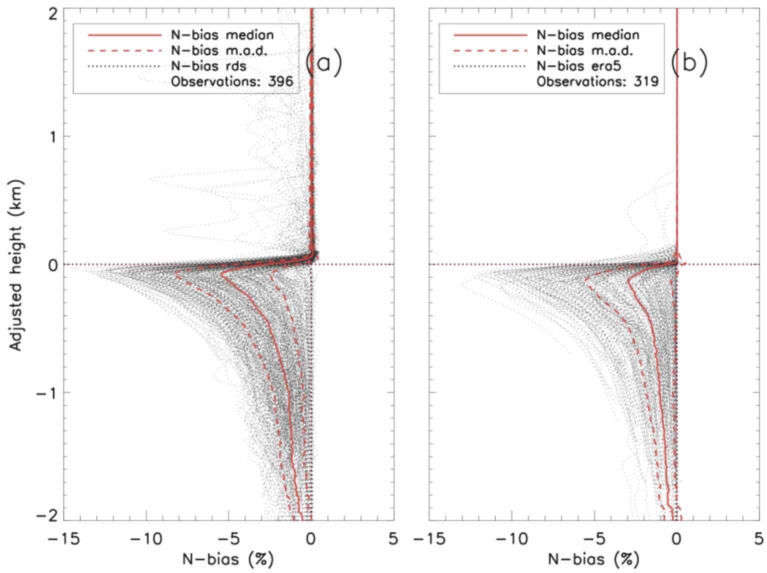

Figure 3.7. Fractional refractivity difference (*N*-bias in %) between the simulated Abel-retrieved refractivity profile and the original observation profile ($(N_{Abel} - N_{Obs})/N_{Obs}$), for all individual observations (dotted gray): (a) MAGIC radiosondes (396 total profiles) and (b) ERA5 (319 total profiles) with population median (solid red) ± MAD (dashed red). Note the zero value in the adjusted height refers to the PBLH for each individual *N*-bias profile.

3.3.4 Zonal variation of the *N*-bias along the transect

To illustrate the large variation in the *N*-bias vertical structure resulting from the spatial variations of ducting height and strength, Fig. 3.8 presents the *N*-bias profiles (median ± MAD) for each 5˚ bin, replacing the zero adjusted height with the median PBLH for each bin. The radiosonde composite (Fig. 3.8a) illustrates the westward transition of the median *N*-bias profiles from the largest peak *N*-bias at ~0.8 km near the coast of Los Angeles, California, to a much reduced peak *N*-bias but higher altitude of ~1.8 km at Honolulu, Hawaii. Table 3.1 lists detailed statistics of the peak *N*-bias values at each bin for both radiosonde and ERA5 data. Although the vertical structure of the *N*-bias profiles along the transect are consistent as seen in Fig. 3.7, significant changes of the *N*-bias magnitude and its peak *N*-bias occurring height along the transect are clearly seen.

The maximum peak *N*-bias (−7.86%) in the radiosonde data is located at the easternmost of the transect near California (−122.5˚E). Whereas the minimum peak *N*-bias (−4.37%) is located near the center of the transect (−147.5˚E). Similarly, the ERA5 also show the maximum peak *N*-bias (−5.92%) near California (−122.5˚E). However, the minimum peak *N*-bias (−0.77%) is found near Hawaii (−157.5˚E). Overall, the *N*-bias in ERA5 are smaller than radiosonde in all bins. However, a noticeable difference exists between the ERA5 and radiosonde profiles for the two westernmost longitude bins (−157.5˚E and −152.5˚E) where the ERA5 reveals a much lower and weaker *N*-bias than the MAGIC data.

Note that the PBLH is above the height of the peak *N*-bias, with a maximum difference of 100 m (−137.5˚E) and a minimum difference of ~15 m (−152.5˚E). Comparatively, the ERA5 PBL height shows greater difference than the height of peak *N*-bias with a maximum difference of 230 m (−142.5˚E) and a minimum of ~45 m (−157.5˚E).

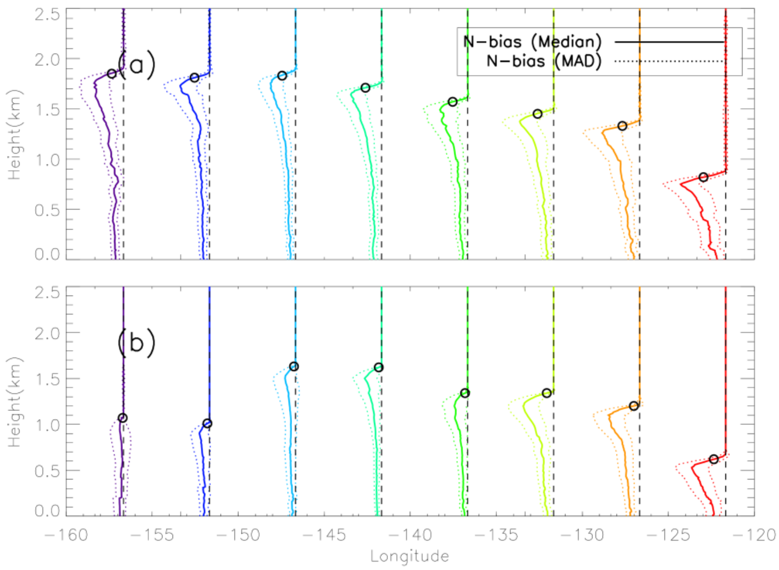

Figure 3.8. Median *N*-bias (solid) ± MAD (dotted) along the north Pacific transect for MAGIC radiosondes (a) and ERA5 (b). Open circles represent the median PBL height for each 5° bin.

Table 3.1. Median and MAD peak *N*-bias values for MAGIC radiosondes (RDS) and ERA5 for each 5° bin.

Peak N-bias				
Longitude	**RDS median**	**RDS MAD**	**ERA5 median**	**ERA5 MAD**
−157.5°	−5.12	±2.61	−0.77	±1.73
−152.5°	−5.10	±2.97	−1.76	±1.61
−147.5°	−4.37	±2.14	−1.83	±2.10
−142.5°	−5.36	±2.53	−2.95	±2.17
−137.5°	−4.82	±2.96	−2.31	±2.14
−132.5°	−5.90	±3.03	−5.31	±2.68
−127.5°	−6.55	±3.40	−5.45	±2.88
−122.5°	−7.86	±3.15	−5.92	±3.04

Figure 3.9 further illustrates the peak *N*-bias, median PBL *N*-bias (0.3 km to PBLH), and the near surface *N*-bias (at 0.3 km) at each bin along the transect. Note the median PBL *N*-bias refer to the median value from the near surface (0.3 km) to the PBLH. Contrary to the general trend of westward decrease in magnitude of the minimum refractivity gradient (Fig. 3.4b) and

ducting strength (Fig. 3.5c), the radiosonde peak *N*-bias shows the maximum (median: −8.10%, MAD: 3.26%) near California (−122.5˚E) and the minimum (median: −4.85%, MAD: 2.18%) over the transition region (−147.5˚E) as well as a slight increase to a secondary maximum (median: −6.11%, MAD: 2.85%) near Hawaii (−157.5˚E). The median PBL *N*-bias and the near surface *N*-bias also show a similar pattern. However, the median *N*-bias demonstrates a sharp decrease in the eastern half of the domain from −5.25% (MAD: 2.71%) at −122.5˚E to −1.71% (MAD: 1.26%) at −137.5˚E, and then remains relatively constant over the western half of the domain. Similarly, the near surface *N*-bias reaches a maximum magnitude of −3.54% (MAD: 2.11%), sharply decreases to −1.06% (MAD: 0.85%) at −137.5˚E, and then remains relatively constant over the western half of the domain.

Note that normalizing each *N*-bias profile to the PBLH preserves the magnitude of the *N*-bias with various heights. Therefore, the relatively large normalized *N*-bias observed near Hawaii indicates more persistent ducting over the trade-cumulus boundary layer regime compared to the transition region in the middle of the transect at -147.5˚E (Fig. 3.8a).

On the other hand, the ERA5 data show a westward decrease of all three *N*-biases, systematically underestimating all three as compared to the radiosondes. This is expected as the decrease of ERA5 vertical resolution at higher altitude leads to a weaker PBL *N*-gradient observation (Fig. 3.4b), and thus weaker ducting and a smaller ducting-induced *N*-bias. Such underestimation of the *N*-bias in the ERA5 minimizes near California where the PBLH is lowest but becomes more severe westward with an increase in height, reaching a maximum magnitude *N*-bias difference near Hawaii. In this case, the peak *N*-bias is merely −0.71% (MAD: 1.80%) as compared to −6.23% (MAD: 2.98%) at −122.5˚E (Fig. 3.9a and Table 3.1). The large difference seen in the *N*-bias along the transect strongly indicates the challenges of the ERA5 data to resolve the sharp gradient across the ducting layer, resulting in a large variation in PBLH of the ERA5 data in the western segment of the region. The increasing difference between the radiosonde and ERA5 data from east to west is most pronounced in the peak *N*-bias cross-section (Fig. 3.9a) but is also evident in both the median *N*-bias (Fig. 3.9b) as well as the near surface *N*-bias (Fig. 3.9c).

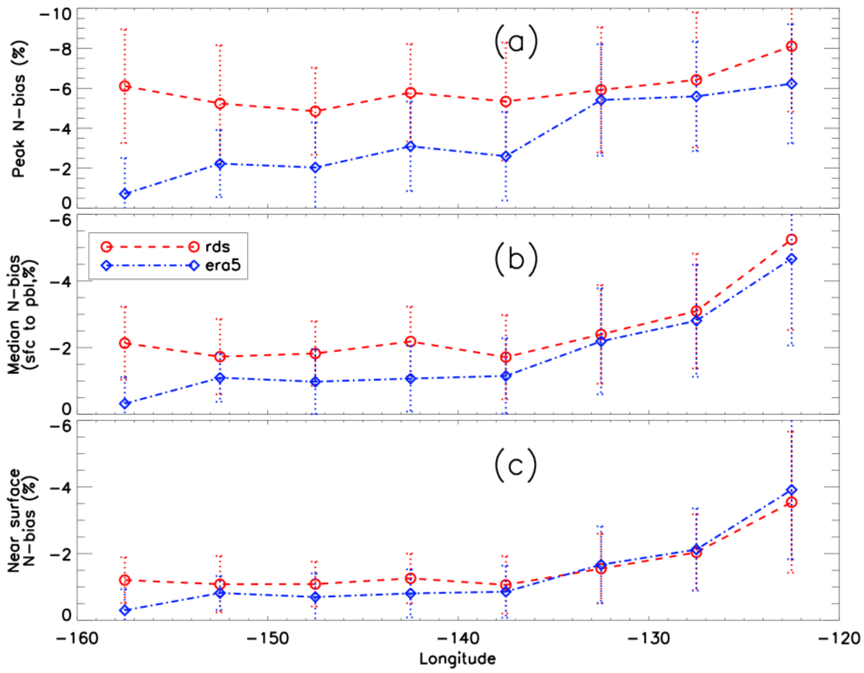

Figure 3.9. Zonal transect of 5° bin (a) peak *N*-bias, (b) median PBL *N*-bias (0.3 km to PBLH), and (c) near surface *N*-bias at 0.3 km for MAGIC (median in red circle and red-dashed line, MAD in red-dotted error bar) and ERA5 (median in blue diamond and dot-dashed line, MAD in blue-dotted error bar).

3.3.5 The *N*-bias and key variable relationship

Figure 3.10 shows a scatter plot of the PBLH vs. height of peak *N*-bias along the transect with each data point colored by the center longitude of the bin to which it belongs. The PBLH and the height of peak *N*-bias show a clear linear relationship with high correlation for both the MAGIC (0.89) and ERA5 (0.98) data. The majority of the radiosonde data show the heights of peak N-bias align well with the PBLH with a very small low bias (less than 80 m). The reason for the lower correlation value in MAGIC data is attributed to outlier cases when the radiosonde N-bias profiles with a double peak at which the larger magnitude bias is located (Fig. 3.7a). On the other hand, the ERA5 maximum ducting heights show little difference from the PBLH near California (e.g., −122.5˚E), but become lower moving westward, which is illustrated by the increasing difference between the linear regression line and the 1:1 line..

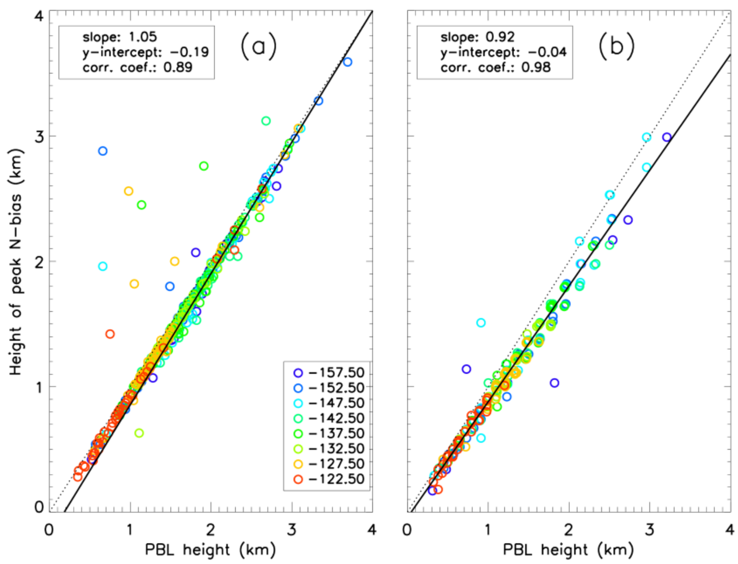

Figure 3.10. PBLH vs. height of maximum *N*-bias for individual profiles from MAGIC (a) and ERA5 (b) data. The color of each open circle represents the center longitude of the 5˚ bin to which each profile belongs.

Figure 3.11 shows a near-linear relationship between the minimum refractivity gradients and the peak N-biases for both MAGIC radiosondes and ERA5 profiles, i.e., the sharper the refractivity gradient, the larger the N-bias. The correlation coefficient for both MAGIC radiosondes (0.93) and the ERA5 profiles (0.88) are also presented. The sharpness parameter (Fig. 3.11c, 3.11d) also shows a linear relationship with the maximum N-bias which is a result of its dependence on the minimum refractivity gradient. Interestingly, their relationship with the peak *N*-bias exhibits no indication of zonal dependence.

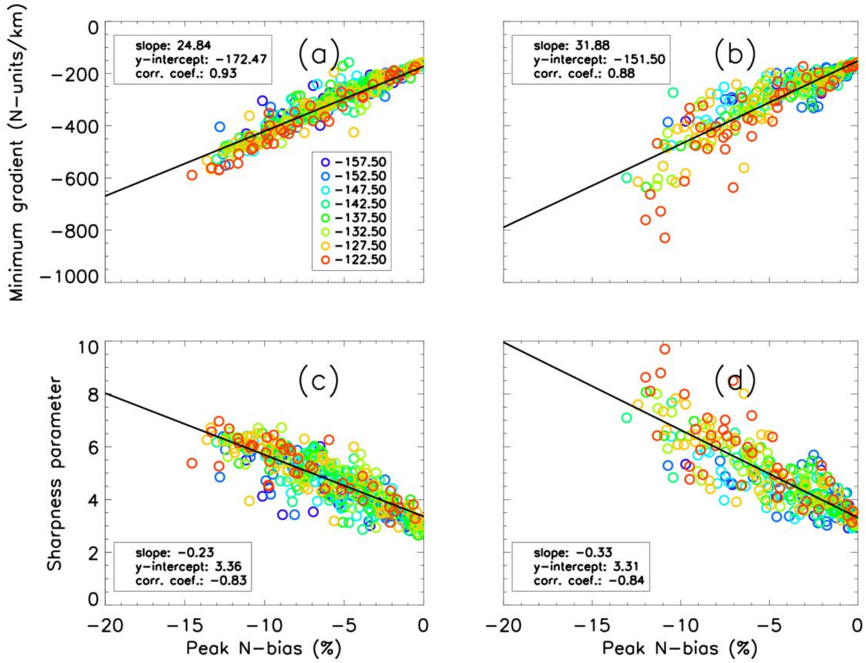

Figure 3.11. (a, b) Minimum refractivity gradient (N-units km^{-1}) and (c, d) sharpness parameter, as a function of the peak *N*-bias (%) for MAGIC (a, c) and ERA5 (b, d) data with the line of linear regression in solid black. Color of each open circle represents the center longitude of the 5° bin to which each profile belongs.

3.4 Summary and conclusions

In this study, radiosonde profiles from the MAGIC field campaign have been analyzed to investigate ducting characteristics and the induced systematic refractivity biases in GNSS RO retrievals over the Northeastern Pacific Ocean between Hawaii and California. Colocated ERA5 model reanalysis data were used as a secondary comparison to the radiosonde observations. The nearly 1-year high-resolution MAGIC radiosonde dataset reveals the frequent presence of ducting marked by a sharp refractivity gradient resulting from the large moisture lapse rate across a strong temperature inversion layer. The PBLH increases by more than 1 km along the transect from California to Hawaii while the magnitude of the refractivity gradient decreases by

100 N-units km−1. The zonal gradient of both variables illustrates the transition of the PBL from shallow stratocumulus adjacent to the California coast to deeper trade-wind cumulus that are prevalent near the Hawaiian Islands.

End-to-end simulation on all radiosonde and ERA5 refractivity profiles has been conducted to estimate the systematic negative N-bias in GNSS RO observations. The ducting layer maintains remarkably consistent thickness (110 m) along the transect with westward decreasing strength and increasing height. The ERA5 slightly underestimates both the height and strength of the ducting layer as well as the PBLH. A systematic negative refractivity bias (N-bias) below the ducting layer is observed throughout the transect, peaking (-5.42%) approximately 80 meters below the PBL height, and gradually decreasing towards the surface (-0.5%). The height of the peak N-bias and the PBLH show a highly positive correlation. The median difference between the two is about 80 meters in the radiosonde but increasing to about 120 meters in the colocated ERA5 data.

MAGIC radiosondes indicate larger values of both ducting strength (ΔN) and thickness (Δh) than ERA5 in the western half of the transect. The opposite is true in the eastern portion of the domain, and is likely associated with the transition of the cloud layer from open-cell cumulus in the west to stratocumulus and stratus in the east (Bretherton et al., 2019; Wood et al., 2011). The ERA5 systematically underestimates the average ducting layer gradient ($\Delta N/\Delta h$) comparing to the radiosondes. The largest N-bias is found over the region with strongest ducting and largest sharpness parameter. It is worth noting that the PBL over the western portion of the transect near Hawaii frequently shows two major gradient layers (a mixing layer at ~1 km and the trade-inversion at ~2 km), with comparable N-gradients (e.g., Fig. 3.2). The much lower PBLH seen in ERA5 in this region is likely due, in part, to the decreasing number of model levels in ERA5 at higher altitude, which could lead to higher possibility of identifying the lower gradient layer as the PBLH. However, the impact of the vertical resolution on the performance of gradient method for PBLH detection has not been performed in this study and warrants more comprehensive study in the future.

3.5 References

Anthes, R. A., and Coauthors: The COSMIC/FORMOSAT-3 Mission: Early Results, *BAMS*, 89, 313–334, doi.org/10.1175/bams-89-3-313, 2008.

Ao, C. O., Meehan T. K., Hajj, G. A., Mannucci, A. J., and Beyerle, G.: Lower Troposphere Refractivity Bias in GPS Occultation Retrievals, *J. Geophys. Res.*, 108, 4577, doi:10.1029/2002JD003216, 2003.

Ao, C. O.: Effect of Ducting on Radio Occultation Measurements: An Assessment Based on High-resolution Radiosonde Soundings, *Radio Sci.*, 42, RS2008, doi.org/10.1029/2006RS003485, 2007.

Ao, C. O., Chan, T. K., Iijima, A., Li, J.-L., Mannucci, A. J., Teixeira, J., Tian, B., and Waliser, D. E.: Planetary Boundary Layer Information from GPS Radio Occultation Measurements, in: *Proceedings of the GRAS SAF Workshop on Applications of GPSRO Measurements*, Vol. 5 of, GRAS SAF Workshop on Applications of GPSRO Measurements, Reading, United Kingdom, ECMWF and EUMETSAT, 123–131, https://www.ecmwf.int/sites/default/files/elibrary/2008/7459-planetary-boundary-layer-information-gps-radio-occultation-measurements.pdf, 16–18 June, 2008.

Ao, C. O., Waliser, D. E., Chan, S. K., Li, J.-L., Tian, B., Xie, F., and Mannucci, A. J.: Planetary boundary layer heights from GPS radio occultation refractivity and humidity profiles, *J. Geophys. Res.*, 117, D16117, doi:10.1029/2012JD017598, 2012.

Basha, G., and Ratnam, M. V.: Identification of atmospheric boundary layer height over a tropical station using high-resolution radiosonde refractivity profiles: Comparison with GPS radio occultation measurements, *J. Geophys. Res.*, 114, doi.org/10.1029/2008jd011692, 2009.

Beyerle, G., Gorbunov, M. E., and Ao, C.O.: Simulation studies of GPS radio occultation measurements, *Radio Sci.*, 38, 1084, doi:10.1029/2002RS002800, 2003.

Bretherton, C.S., and Coauthors: Cloud, Aerosol, and Boundary Layer Structure across the Northeast Pacific Stratocumulus–Cumulus Transition as Observed during CSET, *Mon.Wea. Rev.*, 147, 2083–2102. DOI: 10.1175/MWR-D-18-0281, 2019

Eshleman, V.R.: The radio occultation method for the study of planetary atmospheres, *Planet. Space Sci.*, 21, 1521-1531, doi.org/10.1016/0032-0633(73)90059-7, 1973.

Feng, X., Xie, F., Ao, C.O., and Anthes, R.A.: Ducting and Biases of GPS Radio Occultation Bending Angle and Refractivity in the Moist Lower Troposphere, *J. Atmos. Oceanic Technol.*, 37, 1013–1025, doi.org/10.1175/JTECH-D-19-0206.1. 2020.

Fjeldbo, G., and Eshleman, V.R.: The Atmosphere of Mars Analyzed by Integral Inversion of the Mariner IV Occultation Data, *Planet. Space Sci.*, 16, 1035-1059, doi.org/10.1016/0032-0633(68)90020-2, 1968.

Fjeldbo, G., Kliore, A. J., and Eshleman, V. R.: The neutral atmosphere of Venus as studied with the Mariner V radio occultation experiments, *Astron. J.*, 76, 123– 140, DOI: 10.1086/111096, 1971.

Garratt, J. R.: Review: the atmospheric boundary layer, *Earth-Sci. Rev.*, 37, 89–134, SSDI: 0012-8252(94)00032-R. 1994

Guo, P., Kuo, Y. H., Sokolovskiy, S. V., and Lenschow, D. H.: Estimating Atmospheric Boundary Layer Depth Using COSMIC Radio Occultation Data, *J. Atmos. Sci.*, 68, 1703–1713, doi.org/10.1175/2011jas3612.1, 2011.

Gorbunov, M. E.: Canonical transform method for processing radio occultation data in the lower troposphere, *Radio Sci.*, 37(5), 1076, doi:10.1029/2000RS002592, 2002.

Gorbunov, M. E., Benzon, H. H., Jensen, A.S, Lohmann, M.S., and Nielsen, A.S.: Comparative analysis of radio occultation processing approaches based on Fourier integral operators. *Radio Sci.*, 39, RS6004, https://doi.org/10.1029/2003RS002916, 2004

Healy, S. B.: Radio occultation bending angle and impact parameter errors caused by horizontal refractive index gradients in the troposphere: A simulation study, *J. Geophys. Res*, 106, D11, 11875–11889, doi:10.1029/2001JD900050, 2001.

Hersbach, H., Bell, B., Berrisford, P., Hirahara, S., Horányi, A., Muñoz-Sabater, J., Nicolas, J., Peubey, C., Radu, R., Schepers, D., Simmons, A., Soci, C., Abdalla, S., Abellan, X., Balsamo, G., Bechtold, P., Biavati, G., Bidlot, J., Bonavita, M., De Chiara, G., Dahlgren, P., Dee, D., Diamantakis, M., Dragani, R., Flemming, J., Forbes, R., Fuentes, M., Geer, A., Haimberger, L., Healy, S., Hogan, R. J., Hólm, E., Janisková, M., Keeley, S.,Laloyaux, P., Lopez, P., Lupu, C., Radnoti, G., de Rosnay, P., Rozum, I., Vamborg, F., Villaume, S., and Thépaut, J.-N.: The ERA5 Global Reanalysis, *Q. J. Roy. Meteor. Soc.*, 146, 1999–2049, https://doi.org/10.1002/qj.3803, 2020.

Jensen, A. S., Lohmann, M.S., Nielsen, A.S. and Benzon, H.-H.: Geometrical optics phase matching of radio occultation signals, *Radio Sci.*, 39, RS3009, doi:10.1029/2003RS002899, 2004.

Jensen, A. S., Lohmann, M.S., Benzon, H.-H, and Nielsen, A.S.: Full spectrum inversion of radio occultation signals, *Radio Sci.*, 38(3), 1040, doi:10.1029/2002RS002763, 2003.

Johnston, B. R., Xie, F., and Liu, C.: The effects of deep convection on regional temperature structure in the tropical upper troposphere and lower stratosphere, *J. Geophys. Res.: Atmos.*, 123, 1585−1603, doi.org/10.1002/2017JD027120, 2018.

Klein, S. A., and Hartmann, D. L.: The seasonal cycle of low stratiform clouds, *J. Climate*, 6, 1587−1606, doi:10.1175/1520-0442(1993)006<1587:TSCOLS>2.0.CO;2, 1993.

Kursinski, E. R., Hajj, G. A., Schofield, J. T., Linfield, R. P., and Hardy, K. R.: Observing Earth's atmosphere with radio occultation measurements using the Global Positioning System, *J. Geophys. Res.: Atmos.*, 102, 23429−23465, doi.org/10.1029/97jd01569, 1997.

Kursinski, E. R., G. A. Hajj, Leroy, S. S., and Herman, B.: The GPS Radio Occultation Technique, *Terr. Atmos. Ocean. Sci. (TAO)*, 11, 53−114, 2000.

Lewis, E. R.: Marine ARM GPCI Investigation of Clouds (MAGIC) Field Campaign Report. U.S. Department of Energy, https://doi.org/10.2172/1343577, 2016.

Maddy, E. S. and Barnet, C. D.: Vertical resolution estimates in version 5 of AIRS operational retrievals, *IEEE Transactions on Geoscience and Remote Sensing*, 46, 2375−2384, doi:10.1109/TGRS.2008.917498, 2008.

Nelson, K. J., Xie, F., Ao, C. O., and Oyola-Merced, M. I.: Diurnal Variation of the Planetary Boundary Layer Height Observed from GNSS Radio Occultation and Radiosonde Soundings over the Southern Great Plains, *J. Atmos. Oceanic Tech.*, 38, 2081−2093, https://doi.org/10.1175/jtech-d-20-0196.1, 2021.

Nelson, K. J., Xie, F., Chan, B. C., Goel, A., Kosh, J., Reid, T. G. R., Snyder, C. R., and Tarantino, P. M.: GNSS Radio Occultation Soundings from Commercial Off-the-Shelf

Receivers Onboard Balloon Platforms, *Atmos. Meas. Tech.*, https://doi.org/10.5194/amt-2022-198, 2022.

Painemal, D., Minnis, P., and Nordeen, M.: Aerosol variability, synoptic-scale processes, and their link to the cloud microphysics over the Northeast Pacific during MAGIC, *J. Geophys. Res. Atmos.*, 120, 5122–5139, doi:10.1002/2015JD023175, 2015.

Patterson, W. L.: Climatology of Marine Atmospheric Refractive Effects: A Compendium of the Integrated Refractive Effects Prediction System (IREPS) Historical Summaries. Naval Ocean Systems Center, https://apps.dtic.mil/sti/pdfs/ADA155241.pdf, 1982.

Ramanathan, V., Cess, R. D., Harrison, E. F., Minnis, P., Barkstrom, B. R., Ahmad, E., and Hartmann, D.: Cloud-radiative forcing and climate: Results from the Earth Radiation Budget Experiment, *Science*, 243, 57–63, DOI:10.1126/science.243.4887.57, 1989.

Riehl, H.: Climate and weather in the tropics. London: Academic Press. 611 pp. ISBN 0.12.588180.0, 1979.

Rocken, C., Anthes, R., Exner, M., Hunt, D., Sokolovskiy, S., Ware, R., Gorbunov, M., Schreiner, W., Feng D., Herman B., Kuo, Y.-H., Zou, X.: Analysis and validation of GPS/MET data in the neutral atmosphere, *J. Geophys. Res.*, 102, 29849−29866, https://doi.org/10.1029/97JD02400, 1997.

Schreiner, W. S., Weiss, J.P., Anthes, R.A., Braun, J., Chu, V., Fong, J., Hunt, D., Kuo, Y.-H., Meehan, T., Serafino, W., Sjoberg, J., Sokolovskiy, C., Talaat, E., Wee, T.K., Zeng, Z.: COSMIC-2 Radio Occultation Constellation: First Results, *Geophys. Res. Lett.*, 47, https://doi.org/10.1029/2019gl086841, 2020.

Seidel, D. J., Ao, C.O. and Li, K.: Estimating climatological planetary boundary layer heights from radiosonde observations: Comparison of methods and uncertainty analysis, *J. Geophys. Res.*, 115, D16114, doi:10.1029/2009JD013680, 2010.

Smith, E. K. and Weintraub, S.: The Constants in the Equation for Atmospheric Refractivity Index at Radio Frequencies, *Proc. IRE*, 41, 1035−1037, doi:10.1109/JRPROC.1953.274297, 1953.

Sokolovskiy, S. V.: Modeling and Inverting Radio Occultation Signals in the Moist Troposphere. *Radio Sci.*, 36, 441−458, https://doi.org/10.1029/1999RS002273, 2001.

Sokolovskiy, S. V.: Effect of super refraction on inversions of radio occultation signals in the lower troposphere, *Radio Sci.*, 38 (3), https://doi.org/10.1029/2002RS002728, 2003.

Sokolovskiy, S. V., Kuo, Y.-H., Rocken, C., Schreiner, W. S., Hunt, D. and Anthes, R. A., 2006: Monitoring the atmospheric boundary layer by GPS radio occultation signals recorded in the open-loop mode, *Geophys. Res. Lett.*, 33, L12813, doi:10.1029/2006GL025955, 2006.

Stull, R., Santoso, E., Berg, L. K., and Hacker, J.: Boundary Layer Experiment 1996 (BLX96), *BAMS*, 78, 1149−1158, doi: 10.1175/1520-0477(1997)078<1149:BLEB>2.0.CO;2, 1997.

Stull, R. B.: An Introduction to Boundary Layer Meteorology. Kluwer Academic Publishers, 666 pp., ISBN 90-277-2768-6, 1988.

von Engeln, A. and Teixeira, J.: A Planetary Boundary Layer Height Climatology Derived from ECMWF Reanalysis Data, *J. Climate*, 26, 6575−6590, https://doi.org/10.1175/jcli-d-12-00385.1, 2013.

Winning, T. E., Chen, Y.-L., and Xie, F.: Estimation of the marine boundary layer height over the central North Pacific using GPS radio occultation, *Atmos. Res.*, 183, 362−370, https://doi.org/10.1016/j.atmosres.2016.08.005, 2017.

Wood, R., Mechoso, C. R., Bretherton, C. S., Weller, R. A., Huebert, B., Straneo, F., Albrecht, B. A., Coe, H., Allen, G., Vaughan, G., Daum, P., Fairall, C., Chand, D., Gallardo Klenner, L., Garreaud, R., Grados, C., Covert, D. S., Bates, T. S., Krejci, R., Russell, L.M., de Szoeke, S., Brewer, A., Yuter, S. E., Springston, S. R., Chaigneau, A., Toniazzo, T., Minnis, P., Palikonda, R., Abel, S. J., Brown, W. O. J., Williams, S., Fochesatto, J., Brioude, J., and Bower, K. N.: The VAMOS Ocean-Cloud-Atmosphere-Land Study Regional Experiment (VOCALS-REx): goals, platforms, and field operations, *Atmos. Chem. Phys.*, 11, 627−654, https://doi.org/10.5194/acp-11-627-2011, 2011.

Xie, F., Syndergaard, S., Kursinski, E. R., and Herman, B.M.: An Approach for Retrieving Marine Boundary Layer Refractivity from GPS Occultation Data in the Presence of Super-refraction, *J. Atmos. Oceanic Technol.*, 23, 1629−1644, https://doi.org/10.1175/JTECH1996.1, 2006.

Xie, F., Haase, J. S., and Syndergaard, S.: Profiling the Atmosphere Using the Airborne GPS Radio Occultation Technique: A Sensitivity Study, *IEEE Transactions on Geoscience and Remote Sensing*, 46, 3424−3435, https://doi.org/10.1109/tgrs.2008.2004713, 2008.

Xie, F., Wu, D. L., Ao, C. O., Kursinski, E. R., Mannucci, A. J., and Syndergaard, S.: Super-refraction effects on GPS radio occultation refractivity in marine boundary layers, *Geophys. Res. Lett.*, 37, https://doi.org/10.1029/2010gl043299, 2010.

Xie, F., Wu, D. L., Ao, C. O., Mannucci, A. J., and Kursinski, E. R.: Advances and limitations of atmospheric boundary layer observations with GPS occultation over southeast Pacific Ocean, *Atmos. Chem. Phys.*, 12, 903−918, doi:10.5194/acp-12-903-2012, 2012.

Zhou, X., Kollias, P., and Lewis, E.: Clouds, precipitation and marine boundary layer structure during MAGIC, *J. Climate*, 28, 2420−2442, https://doi.org/10.1175/JCLI-D-14-00320.1, 2015.

4. ASSESSING THE HORIZONTAL INHOMOGENEITY IN THE LOWER TROPOSPHERE AND ITS IMPACT ON GNSS RADIO OCCULTATION RETRIEVALS –A SIMULATION STUDY

4.1 Introduction

The subtropical northeastern Pacific Ocean has long been known for prevailing elevated atmospheric ducting, which is often seen near the height of the PBL height (PBLH) (Lopez 2009; Ao et al., 2007; Xie et al., 2006; von Engeln and Teixeira, 2004) spanning a horizontal extent on the order of thousands of kilometers (Winning et al. 2017; Xie et al. 2010). In the presence of ducting, the steep negative refractivity gradient in the vicinity of the PBLH is typically caused by an atmospheric temperature inversion, a sharp decrease in moisture, or a combination of both. When ducting is present, it results in a large, systematic underestimation of refractivity (N) below the ducting layer (Xie et al. 2006; Sokolovskiy, 2003; Ao et al., 2003).

On the other hand, the east-west transition from shallow stratocumulus-topped PBL near the south coast of California to a much deeper trade-cumulus topped PBL near Hawaii presents strong evidence of horizontal inhomogeneity (HI) in the atmosphere. Such HI could contribute to errors in the RO bending angle and refractivity retrievals as the embedded local spherical symmetry (LSS) assumption in the RO retrieval will be violated.

In order to quantify the effects of HI, a 2-D model of the atmosphere has been created based on a one-year collection of shipborne radiosonde observations over the northeastern Pacific Ocean. In this region, the structure of the PBL is well-known in that the inversion height is at a minimum (< 1 km) adjacent to the California coast and gradually increases westward, reaching a maximum height (near 2 km) approaching the Hawaiian Islands (Winning et al., 2017). The well-known state of the lower troposphere over the observation domain allows the region to be used as a testbed to study the horizontal inhomogeneity that is inherent in the variability of the PBLH.

Given a 2-D atmospheric model, the GNSS RO signal propagation can be efficiently modeled using a multi-phase-screen (MPS) simulation (Ao et al. 2003; Beyerle et al., 2003; Sokolovskiy, 2001). The simulated RO signals can be further processed to retrieve the RO bending angle and refractivity profile given the assumption of a local spherically symmetric atmosphere. Retrieval errors in the simulated RO profile, introduced by the presence of both ducting and HI can therefore be quantified by comparing the simulated RO profile with the 2D atmospheric model.

In order to thoroughly evaluate the impact of horizontal inhomogeneity on RO retrieval, the impact of ducting over the region needs to be separated. Section 4.2 provides details of the 2-D atmosphere model used for this study. Section 4.3 presents the 2-dimensional refractivity field and the horizontal asymmetry inherent in the analytical model. Section 4.4 summarizes the presence of horizontal inhomogeneity, its contribution to the *N*-bias and the comparative effect on the assumption of local spherical symmetry (LSS).

4.2 An atmospheric model derived from radiosonde observations

A collection of high-resolution radiosondes from the Marine Atmospheric Radiation Measurement (ARM) GCSS Pacific Cross Section Intercomparison (GPCI) Investigation of Clouds (MAGIC) are used in this study (Lewis 2016; Zhou et al. 2015). The MAGIC field campaign took place from September 26, 2012 to October 2, 2013 as part of the U.S Department of Energy ARM Program Mobile Facility 2 (AMF2) aboard the Horizon Lines container ship, *Spirit*, which completed 20 round trip passes between Los Angeles, California and Honolulu, Hawaii during the yearlong data collection period (Painemal et al., 2015; Zhou, 2015).

The PBLH over the northeast Pacific Ocean transitions from a shallow stratocumulus-topped regime to a higher, trade-cumulus-topped regime along the GPCI transect (Zhou et al., 2015; Garratt, 1994; Riehl, 1979). This unique transition zone coupled with the large number of observations over a 12-month time frame provides the ground truth for creating a representative model with inherent horizontal inhomogeneity inside the PBL.

4.2.1 A simple 5-segment refractivity model

The presence of ducting, which is reproduced by the 2D analytical model, is comparable in both height and magnitude along the transect to the climatology from which it was created. This unique feature allows for the possibility of the model to be “tuned” in order to observe the effect of various types of ducting and HI on simulated refractivity retrievals.

Building on the work of Sokolovskiy (2001), we propose a 5-segment refractivity model to represent the atmospheric vertical structure along the GPCI transect (see the schematic plot in Figure 4.1).

At GNSS L-band frequencies, the atmospheric refractivity (N in N-units) is derived from the refractive index (n), where $N = (n-1) \times 10^6$ and, in the neutral atmosphere (Kursinski et al., 1997), is a function of the atmospheric pressure (P in hPa), temperature (T in K), and partial pressure of water vapor (P_w in hPa) as presented by Smith and Weintraub (1953) below,

$$N = 77.6\frac{P}{T} + 3.73 \times 10^5\,\frac{P_w}{T^2}. \tag{4.1}$$

Scale analysis reveals that the refractivity profile is dominated by atmospheric pressure; therefore, a general vertical refractivity profile, $N(h)$, can be modeled as an exponential function with a certain scale height (H), such as,

$$N(h)=N(h_0)\exp\left(\frac{(h-h_0)}{H}\right). \tag{4.2}$$

Given the vertical refractivity profile, the scale height can also be estimated by rearranging equation (4.2). However, the vertical mixing inside the PBL results in reduced vertical refractivity gradient (i.e., larger scale height) as compared to the free troposphere (i.e. smaller scale height). Moreover, the transition region across the PBL top experiences a significant increase in refractivity gradient due to the presence of a sharp change in moisture and/or temperature inversion; in turn, the profile can no longer be represented by a solely exponential function with a constant scale height. Instead, this transition can be better represented by adding an arctangent function as shown in Sokolovskiy (2001).

To simplify the analytical model by focusing on the inhomogeneity in the lower troposphere, especially inside PBL, a 5-segment refractivity model is introduced (Fig. 4.1). All segments are represented by an exponential function with different scale heights, except that the transition layer across PBLH is modified by an arctangent function (N2). The boundary layer includes two segments (N_1 and N_2). The free troposphere comprises three segments (N_3, N_4, and N_5). Analysis of the MAGIC radiosonde refractivity profiles shows that the refractivity values at the altitude of 7 km are close to a constant value throughout the transect (e.g., N_{4top} at 7 km, Median: 130.54 *N*-units, MAD: 0.78). The atmosphere above 7 km shows very consistent scale height along the transect and is not expected to introduce significant horizontal inhomogeneity when compared to the lower troposphere. Therefore, a fixed exponential model will be applied to N_5 segment along the transect, and N_4 (6.5 km to 7 km) is the transition between N_3 and N_5 segments.

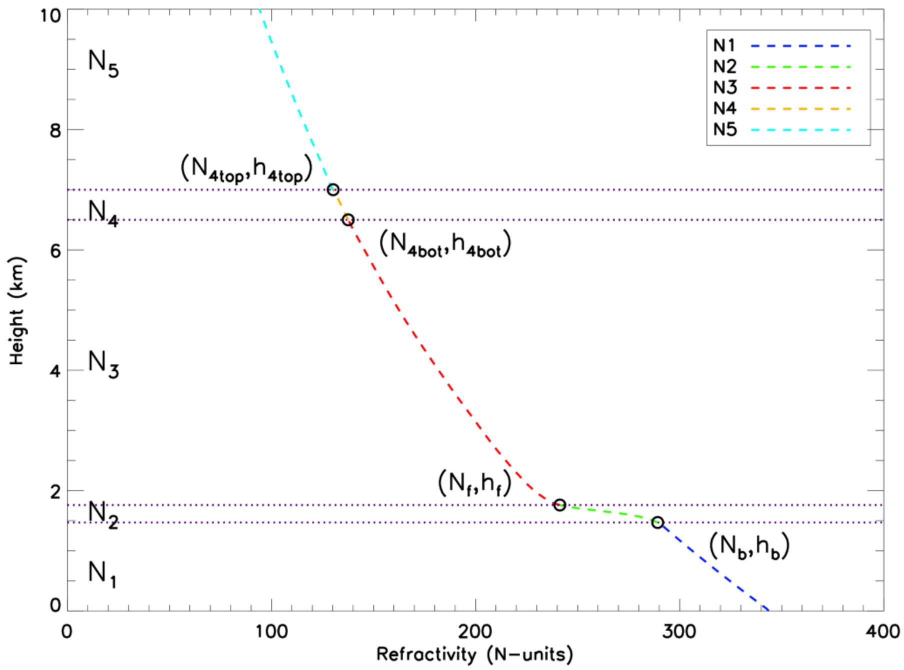

Figure 4.1. Schematic profile of the 5-segment N-model from surface to 10 km. The four dotted lines show the four heights (h_b, h_f, h_{4bot}=6.5 km, h_{4top}=7 km) that separated the 5 segment of the profile. Note the N_5 segment is beyond 10 km. For details about the analytical model, please refer to the Appendix.

To accommodate the large variation of refractivity in the free troposphere, the height dependent scale height $H(h)$, is applied to both N_3 and N_5 segments. However, scalar value scale height (H_1, H_2 and H_4) is used for N_1, N_2 and N_4. Both H_3 and H_5 scale heights are a statistical representation derived from the individual radiosonde profiles. Additional details on the analytical model as well as the scale height can be found in Appendix 1.

4.2.2 The 2D atmospheric refractivity model

Key parameters for the 5-segment model, such as surface refractivity, scale heights, PBL height and its associated minimum gradient and refractivity values etc., are derived from each MAGIC radiosonde. Each parameter is then grouped into eight 5˚ longitudinal bins along the transect (from -160^o to -120^o) as seen in Figure 4.2 (a-d). The median value is calculated for each parameter in every bin, which can be further interpolated into 0.1° longitude interval. Then, an analytical cubic-polynomial-fit function (e.g., $Y=Ax^3+Bx^2+Cx+D$) for each parameter is computed as shown in Figure 4.2 (e-h). In the analytical function for each parameter (Y) is only a function of longitude (i.e., "x") along the transect, where the four coefficients (A, B, C, and D) are constant.

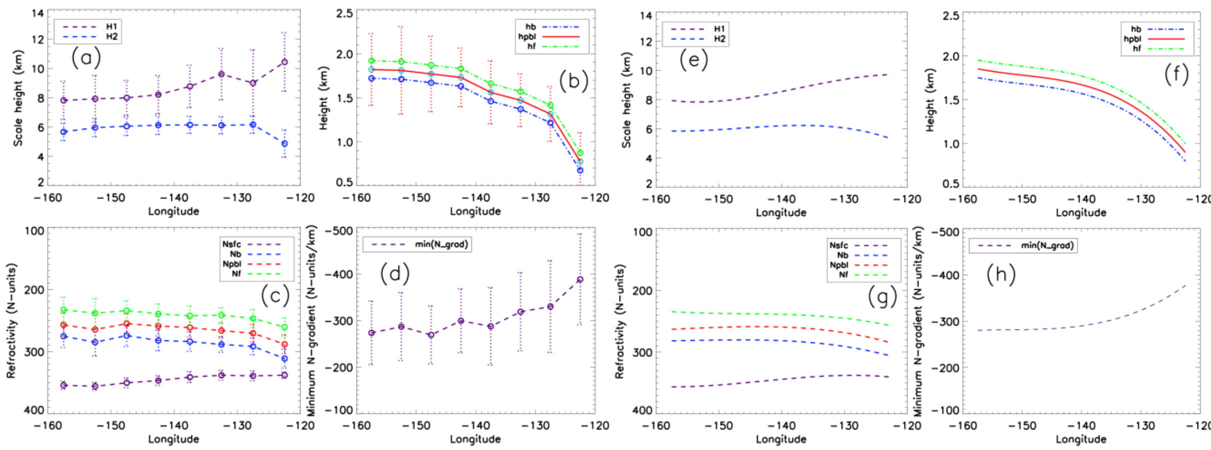

Figure 4.2. (a-d) the median ± median absolute deviation (MAD) of each key parameter of the 5-segment model at 5° longitude bin. (e-h) the corresponding cubic polynomial fit function for each parameter. (a, e): scale height for segment 1 (H_1, purple) and segment 2 (H_2, blue). (b, f): PBL height (h_{PBL}, solid red), bottom of transition layer (h_b, dashed dark blue) and top of transition layer (h_f, dashed green). Note that only MAD of h_{PBL} is shown in (b). (c, g): refractivity values at the surface (N_{sfc}, purple), bottom of transition layer (N_b, dashed blue), PBL height (N_{hPBL}, solid red) and top of transition layer (N_f, dashed green). (d, h): Minimum refractivity gradient.

Figure 4.2 (e-h) shows the analytical function of each key parameter of the 5-segment model as a function of longitude, which preserves the horizontal variation of the atmosphere along the transect. The scale heights and the refractivity values (Fig. 4.2e, g) are constraints for N_1 and N_2 segments of the model profile. The N_2 segment is further constrained by the PBLH and its associated minimum gradient and refractivity value (Fig. 4.2f, h), which will warrant the zonal structure of westward increase of the PBLH and decreasing refractivity gradient magnitude along the transect. The transition layer thickness is predefined as 200 meters centered on the PBLH (e.g., bottom: h_b = PBLH − 100 m, and top: h_f = PBLH + 100 m).

The analytical model with 0.1˚ longitudinal resolution yields the 2-dimensional refractivity field seen in Figure 4.3 preserves the zonal structure across the transect also seen in the MAGIC data.

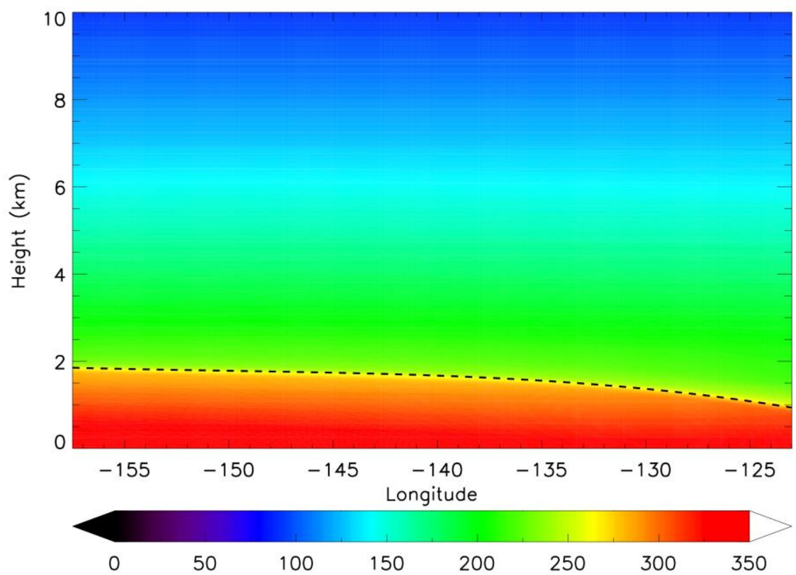

Figure 4.3. The 2-dimensional refractivity field along the transect from surface to 10 km, derived from the N-model with a 0.1˚ longitudinal resolution. The PBLH (black dashed) is identified by the height of the minimum refractivity gradient of the model profiles.

4.2.3 Horizontal inhomogeneity and the asymmetry index

To quantify the magnitude of the horizontal inhomogeneity in a 2D atmosphere, we introduce the asymmetry index (similar to Shaikh et al., 2014), which can be illustrated as the following. First, a midpoint (MPT) at a given longitude and height (*lon, h*) within the domain is identified as the center point of interest. Second, a longitudinal range (Δs) is set by identifying two points on either side of the MPT with equal distance at the same height, i.e., the left boundary point (LBT), and right boundary point (RBT). Third, the horizontal resolution of the 2D atmosphere (*ds*) along the longitude is identified.

Now, the horizontal integrals of *N* from LBT to MPT and from MPT to RBT at the given height (h) are calculated. The absolute difference between the two integrals is defined as the cross sectional asymmetry (CSA, eq. 4.3),

$$CSA(lon, h) = \left|\int_{LBT}^{MPT} N\,(h_i)ds - \int_{MPT}^{RBT} N\,(h_i)ds\right|. \quad (4.3)$$

The sum of the integrals, i.e., the cross sectional total refractivity (CSTR, eq. 4.4) can also be calculated,

$$CSTR(lon, h) = \int_{LBT}^{RBT} N\,(h_i)ds = \int_{LBT}^{MPT} N\,(h_i)ds + \int_{MPT}^{RBT} N\,(h_i)ds. \quad (4.4)$$

Then, the cross section asymmetry index (CSAI, eq. 4.5) at any given point (*lon*, *h*) of the 2D atmosphere is the quotient of CSA and CSTR multiplied by 100 to reflect a fractional value, i.e.,

$$CSAI = \left(\frac{CSA}{CSTR}\right) 10^2. \quad (4.5)$$

Therefore, the larger the CSAI value, the higher horizontal inhomogeneity the 2D atmosphere at the MPT will be. Whereas zero CSAI indicates a horizontally homogeneous atmosphere at the MPT at the given longitude range (Δs). For simplicity, we will use AI (asymmetry index) for CSAI in the manuscript (Shaikh et al., 2014).

In the following example, the horizontal inhomogeneity at the center of the 2D atmosphere is evaluated. The midpoint is set at -140° with the longitude range set as 1.0° with 0.5° at each side of MPT (i.e., LBT at -140.5° and RBT at -139.5°, respectively). Note the horizontal resolution of the 2D model is 0.1° (ds), which results in the use of 11 total points at any given height, e.g., 5 on each side of the MPT without accounting the MPT.

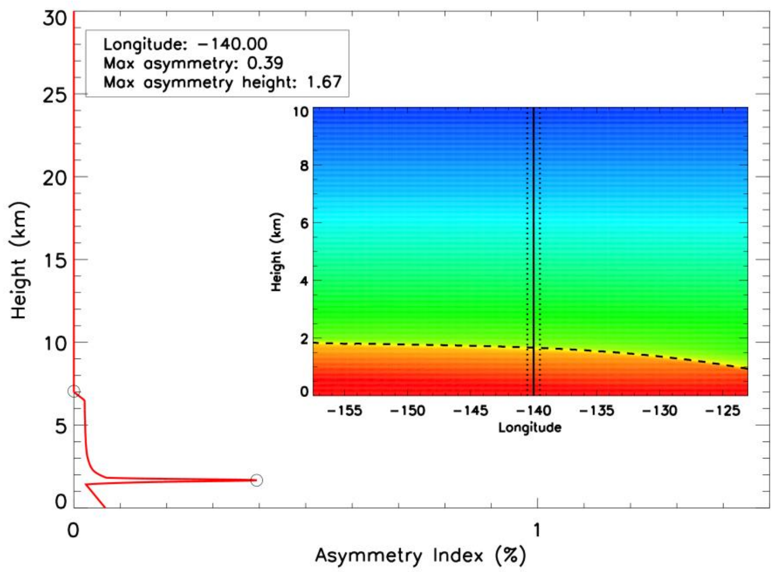

Figure 4.4. Asymmetry index profile at MPT −140˚ with horizonal longitude range set as 1˚ (e.g., MPT ± 0.5˚). Inlay of 2D refractivity model field with 0.1˚ horizontal resolution overlaid with the PBLH (horizontal dashed), midpoint (MPT, vertical solid) and the two boundary points (LBT and RBT, vertical dotted).

Figure 4.4 shows a representative case of the vertical asymmetry profile at the MPT (−140˚), and the 2D analytical refractivity field inlay illustrates the MPT location (solid line) along with the LBT and RBT (dotted lines) equidistant (±0.5˚) from the MPT. In this case, AI is zero above 7 km (e.g., horizontally homogeneous) as expected, and increases at lower altitude reaching the maximum asymmetry value of 0.39% at a height of 1.67 km, where PBLH is located.

Similarly, the asymmetry index calculation can be expanded to the entire 2D refractivity model field spanning the range −157˚ to −123˚ (Fig. 4.5).

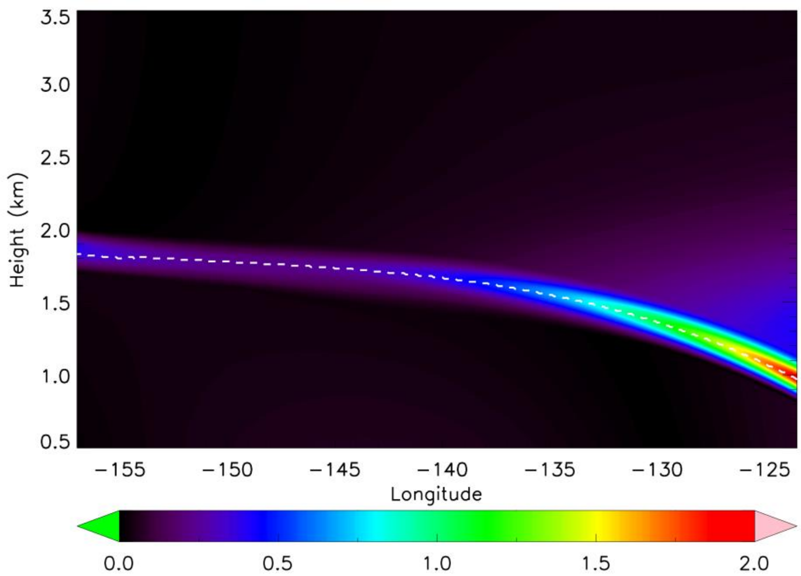

Figure 4.5. Asymmetry index contour of the 2D atmosphere from 0.5 to 3.5 km, overlaid with the PBLH (white dashed line). Values of asymmetry are percentages.

As seen in Figure 4.5, the stronger horizontal inhomogeneity indicated by the large asymmetry index value is seen near the PBLH (dashed-white-line), where the minimum refractivity gradient is located. At any given longitude, the largest asymmetry index occurs about 10 m above the PBLH. In addition, a westward decrease of the AI can be found. The maximum asymmetry index (AI=1.97%) found within the 5˚ to the California coast (near -125˚) are about 1.5 to 2 times the magnitude of the rest of the transect. Moreover, relatively large AI (over 0.25%) is found restricted within about ~100 m of the PBLH (e.g., -157˚ to -135˚), but can reach more than 1 km above PBLH near California coast (-135˚ to -125˚) which is the result of a deeper transition layer and stronger gradients in this region. The residual asymmetry seen adjacent to the coast of California is a result of the variability of the transition layer thickness which can be attributed to the strength of the asymmetry.

The significant asymmetry index (i.e., strong horizontal inhomogeneity) can be attributed to several factors. First, along the transect, the westward increase of the PBLH, where the sharpest refractivity gradient occurs, results in local asymmetry/inhomogeneity occurring around the PBLH. In addition, the slope of the PBLH (e.g., westward increase of PBLH vs longitude) is much steeper in the eastern portion than in the western portion of the transect. The larger PBLH slope further increases the AI. Moreover, the shallower PBLH (< 1 km) near California coast corresponds to larger refractivity, which leads to further increase of AI. The negative correlation between the PBLH slope (in meters per kilometer, m/km) and the PBLH is well illustrated at a 2˚ resolution across the transect (Fig. 4.6), i.e., a steeper PBLH slope at lower PBL heights.

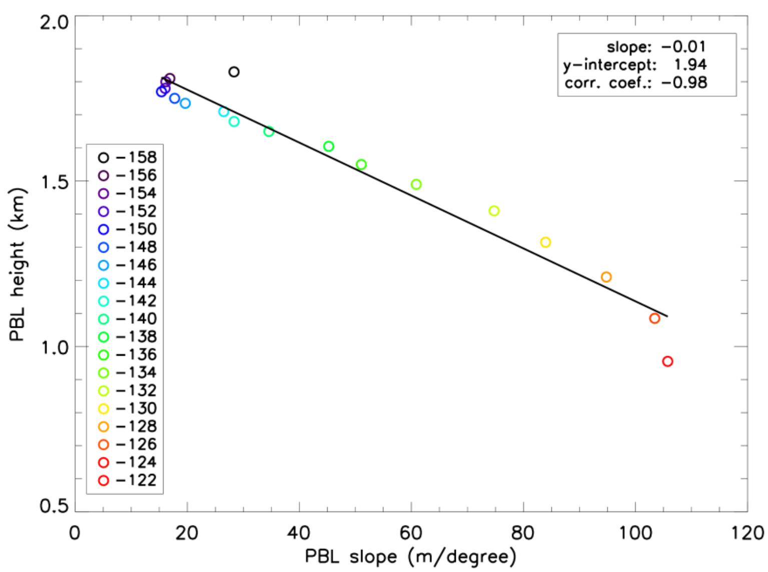

Figure 4.6. Linear regression of 2˚ bin PBLH slope (m/km) vs. PBLH. Open circle colors reference the location (longitude) of observations used to calculate the asymmetry index.

4.3 Simulation study on the 2D atmospheric model

With the horizontal inhomogeneity seen in the previous section, it is interesting to see the difference between a single model profile and its surrounding profiles, which are slightly different due to the absence of AI. Figure 4.7a shows the comparison between the individual refractivity model profile at −140˚ ($N_{\mathrm{m}}(-140^{\circ})$) and the averaged profile within 1˚ surrounding −140˚ ($\overline{N_m} \in (-140.5^{\circ}, -139.5^{\circ})$) and its standard deviation. The fractional difference between the two $((\overline{N_m} - N_m(-140^\circ))/N_m(-140^\circ))$ is overlaid with the 1° asymmetry profile (Fig. 4.7b). The 1.0° averaged profile reflects a minute difference near the PBLH where maximum asymmetry index is observed.

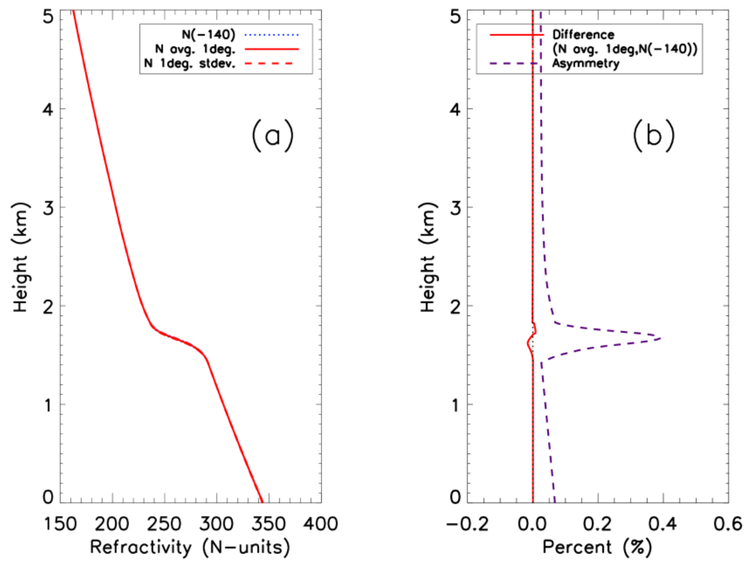

Figure 4.7. (a) Surface to 5 km comparison of $N_m(-140^\circ)$ and average profile of $\overline{N_m}(-140^\circ \pm 0.5^\circ)$ and (b) fractional difference $((\overline{N_m}(-140^\circ \pm 0.5^\circ)$–- $N_m(-140.0^\circ))/N_m(-140.0^\circ))$ (solid red) with 1° asymmetry at −140° (dashed purple) and 1° asymmetry (dashed blue).

In addition to the presence of horizontal inhomogeneity along the transect, the region is well-known for the prevailing ducting condition near PBLH (Feng et al., 2020; Xie et al., 2010; Ao et al., 2007). The presence of inhomogeneity has been acknowledged (Xie et al., 2010; Ao et al., 2007; Xie et al., 2006). Sokolovskiy (2003) demonstrated that the ducting (referred as super-refraction therein) introduced systematic biases in RO refractivity retrieval; whereas, the small-scale horizontal inhomogeneity (2D irregularity) leads to some complication on RO signal tracking but does not introduce any noticeable errors in RO retrievals.

In the following section, we will first evaluate the ducting-induced RO retrieval errors, then, the impact of the large-scale horizontal inhomogeneity along the transect will be quantified with the aid of the multiple phase screen (MPS) simulation.

4.3.1 Assessment of ducting induced *N*-bias

In the presence of ducting, the vertical refractivity gradient exceeds the critical refraction threshold for L-band frequencies (i.e., $dN/dz \leq -157$ N-units km^{-1}). The steep negative refractivity gradient is often observed in the vicinity of the PBLH, which is typically caused by an atmospheric temperature inversion, a moisture lapse, or a combination of both. When ducting is present, the Abel inversion in the standard retrieval process encounters a non-unique inversion problem due to a singularity in the bending angle, resulting in large, systematic underestimation of refractivity below the ducting layer (Xie et al. 2006; Ao et al., 2003; Sokolovskiy, 2003). As discussed in great detail in Xie et al. (2006), in the presence of ducting there exists an infinite number of refractivity profiles that produce the same bending angle profile. As such, the minimum valued solution is used, which leads to the retrieval profile underestimating the true profile (Xie et al., 2006).

The simulation to assess the ducting induced RO refractivity retrieval errors consists of a two-step process adapted from Xie et al. (2006). The first step is to simulate the 1-dimentional GNSS RO bending angle as a function of impact parameter by forward Abel integration of an input refractivity profile. The second step is to simulate the GNSS RO refractivity retrieval by applying the Abel inversion on the simulated bending angle from step one. In the absence of ducting, the impact parameter (i.e., the product of refractive index and the radius of curvature) decreases monotonically with height, allowing a unique solution to the inverse Abel retrieval. However, in the presence of an elevated ducting layer, the Abel retrieval systematically underestimates the refractivity profile due to the non-unique Abel inversion problem resulting from the singularity in bending angle across the ducting layer (Xie et al., 2006; Sokolovskiy, 2003). Following the procedure detailed in Feng et al. (2020), 50 m vertical smoothing has been applied to the simulated bending angle profiles to alleviate the challenge of inverse Abel integration through the very sharp bending angle resulting from strong ducting.

Figure 4.8a shows the input model refractivity profile (N_m) at −140˚ and corresponding Abel refractivity retrieval (N_{Abel}) with the PBLH (1.67 km) marked by a horizontal dotted line. The peak bending angle height corresponds to the sharp refractivity gradient where the PBLH is located (Fig. 4.8c, d). Figure 4.8b shows the fractional *N*-error in the Abel refractivity retrieval. Considering the significant spatial and temporal variations of ducting height along the transect, the height of each fractional *N*-error profile is normalized by its PBLH for easier comparison. For example, the zero value in adjusted height refers to the PBLH for each individual *N*-error profile. The systematic negative *N*-error is clearly shown below the ducting layer marked by the PBLH, with the largest magnitude bias close to the ducting height (median: −5.90%, MAD: 0.78) and a minimum magnitude (median: ~1.2%) near the surface. The composite fractional refractivity difference profiles for all N_m along the transect (Fig 4.8e) can be readily split into three groups. The smallest *N*-biases are located in the middle section of the transect between −135˚ and −145˚. The largest *N*-biases occur in the eastern section near the California coast (−122.5˚to −134.5˚). Finally, the *N*-bias of the western section near Hawaii (−145.1˚to −157.5˚) falls in the middle and aligns best with the median fractional *N*-bias profile for the transect.

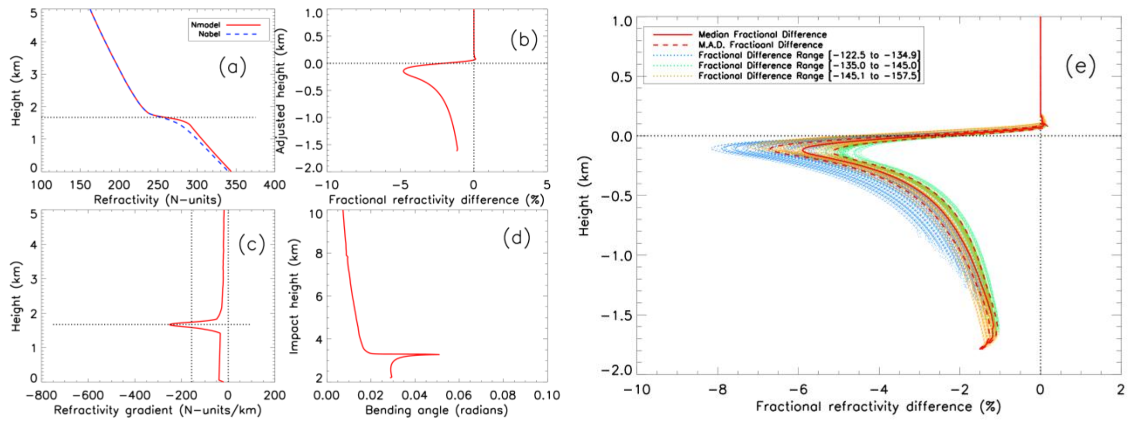

Figure 4.8. (a) The model profile N_m at -140° (solid red) and N_{Abel} (dashed blue); (b) fractional N-bias $((N_{Abel}-N_m)/N_m)$; (c) vertical refractivity gradient of N_m profile; (d) bending angle vs. impact height. (e) Composite *N*-bias of all model profiles with median (solid red) and median absolute deviation (dashed red). The profiles are separated into three groups: longitude 122.5°-134.9° (blue dotted), 135.0°-145.0° (green dotted), 145.1°-157.5° (gold dotted).

4.3.2 Multiple phase screen (MPS) simulation of the 2D atmosphere

The signal propagation for GNSS occultation through a 2D atmosphere can be modeled using the MPS method, which represents the Fourier split step solution of the parabolic wave equation (Levy, 2000). In this method, the atmosphere is approximated by a series of phase screens between which the signal propagates in a vacuum. Unlike ray tracing, MPS includes full-wave diffraction effects and requires no special treatment for multipath. Multipath effects, caused mainly by the existence of water vapor in the lower troposphere, occur when the bending angle cannot be derived directly from the instantaneous frequency of the related signal (Jensen et al., 2004). This occurrence causes the received frequency to be related to a number of pairs of bending angle and impact parameter instead of a single pair (Jensen et al., 2004). Computational parameters, including the distance between phase screens as well as the spacing between discretization points in each phase screen are adjustable according to the needs for model resolution. Its implementation in the context of GNSS RO has been well documented (e.g., Ao et al. 2003; Beyerle et al., 2003; Sokolovskiy, 2001). The model atmosphere is then partitioned into finite screens, each encompassing the property of the interpolated model atmosphere at that point. The simulated GNSS signal is altered by the refractivity value at each point on the screen, while assuming the wave propagates through a vacuum between each screen. The simulated RO signal amplitude and excess phase can then be used to derive the bending angle through the phase matching retrieval (Wang, 2020; Jenson, 2004). The refractivity can therefore be retrieved through the Abel inversion.

4.3.3 Assessment of the impact of horizontal inhomogeneity on RO refractivity retrievals

The MPS is used to simulate GNSS RO signals passing through two separate representations of the model atmosphere: one with 1D (N_{1D}) model atmosphere representing a horizontally homogeneous or spherically symmetric atmosphere; and the second one with the 2D (N_{2D}) model atmosphere with a horizontally inhomogeneous atmosphere (e.g., Fig. 4.4, 4.5). Given the simulated RO signals from the MPS, the bending angle and then refractivity can be retrieved (i.e., N_{1D_Abel} and N_{2D_Abel}). It is worth noting that the bending angle retrieval based on the MPS simulation with the 1D atmosphere will be identical to the geometric optics forward Abel integration of the N_{1D} (Sect. 4.3.1). The 1D retrieval (N_{1D_Abel}) will be negatively biased compared to the N_{1D} in the presence of the ducting (e.g., Fig. 4.8b, e). The impact of the horizontal inhomogeneity on the RO retrieval can therefore be quantified as the retrieved refractivity difference between the 2D and the 1D simulations, i.e., (N_{2D_Abel}-N_{1D_Abel}/N_{1D_Abel}).

Here, three MPS simulations are carried out based on the 2D atmosphere in Section 4.2.2 considering the different level of horizontal inhomogeneity (asymmetry index). The first case uses the 2D atmosphere centered at −134˚ longitude, with the maximum asymmetry index AI=0.83% near the PBLH at 1.53 km; the second case centered at −140˚ with maximum AI=0.45% near the PBLH at 1.67 km (e.g., Fig. 4.4); and the third case centered at −146˚ with maximum AI=0.27% near the PBLH at 1.76 km. It is worth noting the slightly increase in PBL height and decrease in AI for the three centered model profiles.

Figure 4.9 illustrates the fractional refractivity difference profiles (N_{2D_Abel}−N_{1D_Abel}/N_{1D_Abel}) and the corresponding 2D model asymmetry index at the three longitudes. The shaded region highlights the 500 m layer near surface which is excluded from the analysis due to the likely contamination of the RO signal as a result of surface reflection in the MPS simulation.

It is seen that horizontal inhomogeneity leads to negative errors in the GNSS RO refractivity retrievals with maximum magnitude errors for each longitude at similar heights as the maximum AI. Moreover, the larger the asymmetry index (0.83% at −134˚), the larger the negative errors will be (−1.43%). We expect the larger AI (~2%) near the California coast (Fig. 4.5) will lead to even larger errors in RO refractivity retrieval. Second, the height of the maximum fractional difference is higher than the height of maximum asymmetry by 80 m at −134˚, 120 m at −140˚, and 110 m at −146˚.

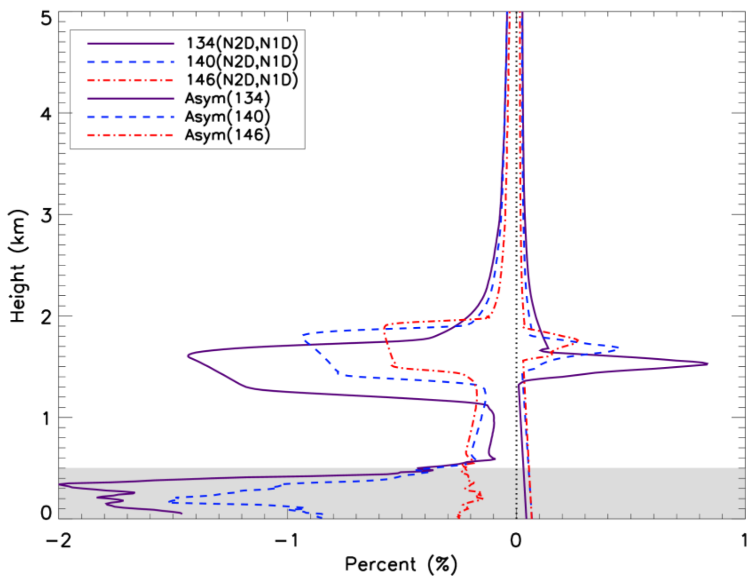

Figure 4.9. Comparison of (2D,1D) fractional difference (N_{2D}-N_{1D}/N_{1D}) (negative profiles) and asymmetry (positive profiles) from surface to 5 km at −134° (solid purple), −140° (dashed blue) and −146° (dot dash red).

4.4 Conclusion

In this paper, a 2-D refractivity model was created based on high resolution radiosonde data from MAGIC field campaign over the northeastern Pacific Ocean, where prevailing ducting and large-scale horizontal inhomogeneity are observed. The asymmetry index is also introduced to quantify the levels of horizontal inhomogeneity. An end to end simulation study shows a negative *N*-bias between −4 and −8% due to the presence of the PBL ducting layer. Further, the bias was greatest over the eastern portion of the GPCI transect and least over the western portion.

The 2D model was then used as input to a MPS simulation in order to differentiate horizontal inhomogeneity from ducting and their respective contribution to the GNSS RO retrievals. Three cases representing slightly different horizontal inhomogeneity were carried out. The results demonstrated that horizontal inhomogeneity could contribute more than 1% to the *N*-bias in the region where the refractivity gradient (and asymmetry index) is strongest. Further, it was shown that as the gradient decreases (i.e. from east to west across the GPCI transect), the horizontal inhomogeneity follows suit. These findings are significant as they represent the first time the impact of large-scale horizontal inhomogeneity on the GNSS RO refractivity retrievals can be quantified.

Finally, the simple 2D model provides a key component of asymmetry and inhomogeneity analysis as its many variables can be easily "tuned" to simulate different structures of the atmosphere. In conjunction with the MPS simulation, numerous scenarios of ducting and inhomogeneity can be modeled to provide an accurate assessment of their presence and contribution to the GNSS retrieval bias. This research enhances understanding of RO data quality within the PBL, which could benefit RO data assimilation and advance weather and climate prediction capabilities.

4.5 References

Anthes, R. A., and Coauthors: The COSMIC/FORMOSAT-3 Mission: Early Results, *BAMS*, 89, 313–334, doi.org/10.1175/bams-89-3-313, 2008.

Ao, C. O., Meehan T. K., Hajj, G. A., Mannucci, A. J., and Beyerle, G.: Lower Troposphere Refractivity Bias in GPS Occultation Retrievals, *J. Geophys. Res.*, 108, 4577, doi:10.1029/2002JD003216, 2003.

Ao, C. O.: Effect of Ducting on Radio Occultation Measurements: An Assessment Based on High-resolution Radiosonde Soundings, *Radio Sci.*, 42, RS2008, doi.org/10.1029/2006RS003485, 2007.

Ao, C. O., Chan, T. K., Iijima, A., Li, J.-L., Mannucci, A. J., Teixeira, J., Tian, B., and Waliser, D. E.: Planetary Boundary Layer Information from GPS Radio Occultation Measurements, in: *Proceedings of the GRAS SAF Workshop on Applications of GPSRO*

Measurements, Vol. 5 of, GRAS SAF Workshop on Applications of GPSRO Measurements, Reading, United Kingdom, ECMWF and EUMETSAT, 123–131, https://www.ecmwf.int/sites/default/files/elibrary/2008/7459-planetary-boundary-layer-information-gps-radio-occultation-measurements.pdf, 16-18 June, 2008.

Ao, C. O., Waliser, D. E., Chan, S. K., Li, J.-L., Tian, B., Xie, F., and Mannucci, A. J.: Planetary boundary layer heights from GPS radio occultation refractivity and humidity profiles, *J. Geophys. Res.*, 117, D16117, doi:10.1029/2012JD017598, 2012.

Beyerle, G., Gorbunov, M. E., and Ao, C.O.: Simulation studies of GPS radio occultation measurements, *Radio Sci.*, 38, 1084, doi:10.1029/2002RS002800, 2003.

Feng, X., Xie, F., Ao, C.O., and Anthes, R.A.: Ducting and Biases of GPS Radio Occultation Bending Angle and Refractivity in the Moist Lower Troposphere, *J. Atmos. Oceanic Technol.*, 37, 1013-1025, doi.org/10.1175/HTECH-D-19-0206.1, 2020.

Garratt, J. R.: Review: the atmospheric boundary layer, Earth-Sci. Rev., 37, 89–134, 1994

Jensen, A. S., Lohmann, M.S., Benzon, H.-H, and Nielsen, A.S.: Full spectrum inverstion of radio occultation signals, *Radio Sci.*, 38(3), 1040, doi:10.1029/2002RS002763, 2003.

Jensen, A. S., Lohmann, M.S., Nielsen, A.S. and Benzon, H.-H.: Geometrical optics phase matching of radio occultation signals, *Radio Sci.*, 39, RS3009, doi:10.1029/2003RS002899, 2004.

Johnston, B. R., Xie, F., and Liu, C.: The effects of deep convection on regional temperature structure in the tropical upper troposphere and lower stratosphere, *J. Geophys. Res.: Atmos.*, 123, 1585-1603, doi.org/10.1002/2017JD027120, 2018.

Kursinski, E. R., Hajj, G. A., Schofield, J. T., Linfield, R. P., and Hardy, K. R.: Observing Earth's atmosphere with radio occultation measurements using the Global Positioning System, *J. Geophys. Res.: Atmos.*, 102, 23429–23465, doi.org/10.1029/97jd01569, 1997.

Kursinski, E. R., G. A. Hajj, Leroy, S. S., and Herman, B.: The GPS Radio Occultation Technique, *Terr. Atmos. Ocean. Sci. (TAO)*, 11, 53–114, 2000.

Levy, M.: Parabolic equation methods for electromagnetic wave propagation. The Institution of Electrical Engineers, London, 2000.

Lewis, E. R.: Marine ARM GPCI Investigation of Clouds (MAGIC) Field Campaign Report. U.S. Department of Energy, https://doi.org/10.2172/1343577, 2016.

Lopez, P., 2009: A 5-yr 40-km-resolution global climatology of superrefraction for ground-based weather radars, *J. Appl. Meteor. Climatol.*, 48, 89–110, https://doi.org/10.1175/2008JAMC1961.1.

Nelson, K. J., Xie, F., Ao, C. O., and Oyola-Merced, M. I.: Diurnal Variation of the Planetary Boundary Layer Height Observed from GNSS Radio Occultation and Radiosonde Soundings over the Southern Great Plains, *J. Atmos. Oceanic Tech.*, 38, 2081–2093, https://doi.org/10.1175/jtech-d-20-0196.1, 2021.

Nelson, K. J., Xie, F., Chan, B. C., Goel, A., Kosh, J., Reid, T. G. R., Snyder, C. R., and Tarantino, P. M.: GNSS Radio Occultation Soundings from Commercial Off-the-Shelf Receivers Onboard Balloon Platforms, *Atmos. Meas. Tech.*, https://doi.org/10.5194/amt-2022-198, 2022.

Painemal, D., Minnis, P., and Nordeen, M.: Aerosol variability, synoptic-scale processes, and their link to the cloud microphysics over the northeast Pacific during MAGIC, *J. Geophys. Res. Atmos.*, 120, 5122–5139, doi:10.1002/2015JD023175, 2015.

Riehl, H.: Climate and weather in the tropics. London: Academic Press. 611 pp. ISBN 13: 9780125881807. 1979.

Shaikh, M.M., Notarpietry, R. and Nava, B.: The impact of the spherical symmetry assumption on RO data inversion in the ionosphere: An assessment study, *Advances in Space Research*, 53, 599-608. Doi: 10.1016/j.asr.2013.10.025. 2014

Smith, E. K. and Weintraub, S.: The Constants in the Equation for Atmospheric Refractivity Index at Radio Frequencies, *Proc. IRE*, 41, 1035-1037, doi:10.1109/JRPROC.1953.274297, 1953.

Sokolovskiy, S. V.: Modeling and Inverting Radio Occultation Signals in the Moist Troposphere, *Radio Sci.*, 36, 441-458, https://doi.org/10.1029/1999RS002273, 2001.

Sokolovskiy, S. V.: Effect of super refraction on inversions of radio occultation signals in the lower troposphere, *Radio Sci.*, 38 (3), https://doi.org/10.1029/2002RS002728, 2003.

Sokolovskiy, S. V., Kuo, Y.-H., Rocken, C., Schreiner, W. S., Hunt, D. and Anthes, R. A., 2006: Monitoring the atmospheric boundary layer by GPS radio occultation signals recorded in the open-loop mode, *Geophys. Res. Lett.*, 33, L12813, doi:10.1029/2006GL025955, 2006.

von Engeln, A. and Teixeira, J.: A ducting climatology derived from the European Centre for Medium-Range Weather Forecasts global analysis fields, *J. Geophys. Res.*, 109, D18104, https://doi.org/10.1029/2003JD004380.2004

Wang, K.-N., Ao, C.O., and de la Torrre Juarez, M.: GNSS-RO refractivity bias correction under ducting layer using surface-reflection signal, *Remote Sensing*, 12, 35,doi:10.3390/rs12030359. 2020

Winning, T. E., Chen, Y.-L., and Xie, F.: Estimation of the marine boundary layer height over the central North Pacific using GPS radio occultation, *Atmos. Res.*, 183, 362–370, https://doi.org/10.1016/j.atmoductinges.2016.08.005, 2017.

Winning, T.E., Xie, F., Nelson, K.J.: Assessing the ducting phenomenon and its impact on GNSS radio occultation refractivity retrievals over the northeast Pacific Ocean using radiosondes and global reanalysis, *Atmos. Meas. Tech.*, In Review. 2023.

Xie, F., Syndergaard, S., Kursinski, E. R., and Herman, B.M.: An Approach for Retrieving Marine Boundary Layer Refractivity from GPS Occultation Data in the Presence of Super-refraction, *J. Atmos. Oceanic Technol.*, 23, 1629-1644, https://doi.org/10.1175/JTECH1996.1, 2006.

Xie, F., Haase, J. S., and Syndergaard, S.: Profiling the Atmosphere Using the Airborne GPS Radio Occultation Technique: A Sensitivity Study, *IEEE Transactions on Geoscience and Remote Sensing*, 46, 3424–3435, https://doi.org/10.1109/tgrs.2008.2004713, 2008.

Xie, F., Wu, D. L., Ao, C. O., Kursinski, E. R., Mannucci, A. J., and Syndergaard, S.: Super-refraction effects on GPS radio occultation refractivity in marine boundary layers, *Geophys. Res. Lett.*, 37, https://doi.org/10.1029/2010gl043299, 2010.

Xie, F., Wu, D. L., Ao, C. O., Mannucci, A. J., and Kursinski, E. R.: Advances and limitations of atmospheric boundary layer observations with GPS occultation over southeast Pacific Ocean, *Atmos. Chem. Phys.*, 12, 903-918, doi:10.5194/acp-12-903-2012, 2012.

Zhou, X., Kollias, P., and Lewis, E.: Clouds, precipitation and marine boundary layer structure during MAGIC, *J. Climate*, 28, 2420-2442, https://doi.org/10.1175/JCLI-D-14-00320.1, 2015.

5. SUMMARY AND CONCLUSION

5.1 Summary

Under climatological conditions, the transition from a shallow stratocumulus-topped PBL to a higher, trade-cumulus boundary layer regime make the region over the Northeastern Pacific Ocean an ideal natural laboratory for observation and analysis of the PBL. While the PBL height varies on both a spatial and temporal scale in absence of an anomalous weather disturbance, the variations are on a local scale and can be seen in the sharp transition between the PBL and the free atmosphere. In the past, this transition could only be detected via radiosonde. Over the open ocean, the conventional microwave and infrared satellite sounders do not provide adequate vertical resolution to depict the height and strength of the PBL inversion layer; whereas radiosonde observations are not available in volume and areal coverage to present a full picture. The launch of the first COSMIC Constellation in 2006 allowed for atmospheric profiling with 100 m vertical resolution to be extended over the open ocean using the GNSS radio occultation technique, enabling large scale PBL observation over the Northeastern Pacific for the first time.

By using the height of the minimum refractivity gradient as a proxy for the PBLH, it was observed that the structure of the PBL undergoes seasonal variation where the area of lowest observed PBL height near the California coast is much larger during the winter months than the summer months. The transition from low PBLH in the east to higher heights in the west is always present; however, the horizontal variability not only exists on a seasonal scale, but on a daily and even a local scale.

The presence of the sharp transition between the boundary layer and free atmosphere that allows for the observation of the PBL can lead to other types of variability. The ducting caused by the vertical moisture gradient can lead to retrieval errors that cause an underestimation of the

Abel retrieved refractivity profile. To estimate the systematic negative *N*-bias in GNSS RO observations from a set of colocated data sets (radiosondes and global reanalysis) due to ducting, we applied an end-to-end simulation on all refractivity profiles that contained at least one elevated ducting layer. The retrieved refractivity profiles were then compared to the input profiles to evaluate the ducting induced *N*-bias.

A comparative analysis between the collection of radiosondes and global reanalysis were used to further investigate the presence of the *N*-bias due to ducting; the peak median value of the *N*-bias for radiosondes is −5.42% (MAD, 2.92%), nearly twice the ERA5 value of −2.96% (MAD, 2.59%).

For the individual bin *N*-bias, the height of the maximum *N*-bias and the PBLH show a highly positive correlation where the refractivity gradient is strongest. The mean difference between the two is about 80 meters in the radiosonde data but increases to about 120 meters in the colocated ERA5 data. The correlation between the PBLH and the height of the maximum *N*-bias is highly positive.

Estimating horizontal inhomogeneity and its impact on GNSS RO soundings is achieved by creating a 2-D statistical refractivity model from high resolution radiosonde data. A negative *N*-bias between −4% and −8% between model input profiles and their corresponding Abel retrievals from the end to end simulation was revealed. The model was then used as input to a MPS simulation in order to differentiate horizontal inhomogeneity from ducting and their respective contribution to the *N*-bias. In order to achieve this, the MPS simulation was performed twice at the same center point; the first iteration of the retrieval was through a homogeneous atmosphere the second through an inhomogeneous atmosphere created with the 2 dimensional model. The results demonstrated that horizontal inhomogeneity contributes more than 1% to the

N-bias in the region where the refractivity gradient is strongest. Further, it was shown that as the gradient decreases the inhomogeneity follows suit. These findings are significant as this is the first time the presence of HI can be quantified and provide a proxy (asymmetry) that can be used as an estimation.

5.2 Conclusion

The simple 2D model provides a key component of asymmetry and horizontal inhomogeneity analysis as its many variables can be “tuned” to represent different PBL structures over different regions. When the 2D model is used in conjunction with the MPS simulation, numerous scenarios of both ducting and inhomogeneity can be modeled and a more thorough assessment of their contribution to the GNSS RO retrieval bias can be achieved.

This dissertation research enhances understanding of RO data quality within the PBL, paving the way for improved RO data assimilation and advancing weather and climate prediction capabilities.

5.3 References

Ao, C. O., Meehan T. K., Hajj, G. A., Mannucci, A. J., and Beyerle, G.: Lower Troposphere Refractivity Bias in GPS Occultation Retrievals, *J. Geophys. Res.*, 108, 4577, doi:10.1029/2002JD003216, 2003.

Ao, C. O.: Effect of Ducting on Radio Occultation Measurements: An Assessment Based on High-resolution Radiosonde Soundings, *Radio Sci.*, 42, RS2008, doi.org/10.1029/2006RS003485, 2007.

Ao, C. O., Waliser, D. E., Chan, S. K., Li, J.-L., Tian, B., Xie, F., and Mannucci, A. J.: Planetary boundary layer heights from GPS radio occultation refractivity and humidity profiles, *J. Geophys. Res.*, 117, D16117, doi:10.1029/2012JD017598, 2012.

Basha, G., and Ratnam, M. V.: Identification of atmospheric boundary layer height over a tropical station using high-resolution radiosonde refractivity profiles: Comparison with GPS radio occultation measurements, *J. Geophys. Res.*, 114, doi.org/10.1029/2008jd011692, 2009.

Beyerle, G., Gorbunov, M. E., and Ao, C.O.: Simulation studies of GPS radio occultation measurements, *Radio Sci.*, 38, 1084, doi:10.1029/2002RS002800, 2003.

Healy, S. B.: Radio occultation bending angle and impact parameter errors caused by horizontal refractive index gradients in the troposphere: A simulation study, *J. Geophys. Res.*, 106, D11, 11875–11889, doi:10.1029/2001JD900050, 2001.

Levy, M.: Parabolic equation methods for electromagnetic wave propagation. The Institution of Electrical Engineers, London, 2000.

Sokolovskiy, S. V.: Modeling and Inverting Radio Occultation Signals in the Moist Troposphere. *Radio Sci.*, 36, 441−458, https://doi.org/10.1029/1999RS002273, 2001.

Sokolovskiy, S. V.: Effect of super refraction on inversions of radio occultation signals in the lower troposphere, *Radio Sci.*, 38 (3), https://doi.org/10.1029/2002RS002728, 2003.

Stull,R.B., 2000. Meteorology for Scientists and Engineers. 2nd ed. Brooks/Cole 502 pp.

Winning, T. E., Chen, Y.-L., and Xie, F.: Estimation of the marine boundary layer height over the central North Pacific using GPS radio occultation, *Atmos. Res.*, 183, 362−370, https://doi.org/10.1016/j.atmosres.2016.08.005, 2017.

Xie, F., Syndergaard, S., Kursinski, E. R., and Herman, B.M.: An Approach for Retrieving Marine Boundary Layer Refractivity from GPS Occultation Data in the Presence of Super-refraction, *J. Atmos. Oceanic Technol.*, 23, 1629-1644, https://doi.org/10.1175/JTECH1996.1, 2006.

Xie, F., Wu, D. L., Ao, C. O., Mannucci, A. J., and Kursinski, E. R.: Advances and limitations of atmospheric boundary layer observations with GPS occultation over southeast Pacific Ocean, *Atmos. Chem. Phys.*, 12, 903-918, doi:10.5194/acp-12-903-2012, 2012.

Zeng, Z., Sokilovskiy, S., Schreiner, W., Hunt, D., Lin,.J., and Kuo, Y.-H.: Ionospheric correction of GPS radio occultation data in the troposphere. *Atmos. Meas. Tech.*, **9**, 335-346, 2016.

APPENDIX: THE 5-SEGMENT REFRACITIVY MODEL

Segment one (N_1) begins with the key variable for the surface refractivity (N_{sfc}) at the first element of the altitude array (h = 0.01 m). The scale height H_1 (A.13) is a scalar value for the N_1 segment,

$$N_1(h_i)=N_{sfc}*\exp\left(\frac{(-h_i)}{H1}\right) \qquad h_i \le h_b. \tag{A.1}$$

The leading coefficient N_0 is determined at the key variable point (N_{PBL}, h_{PBL}) (e.g. $N_{PBL}(h_{PBL})=N_0*\exp\left(\frac{(-h_{PBL})}{H2}\right)$) (eq. A.3). The scale height H_2 (A.14) is a scalar value.

$$N_2(h_i)= N_0*\exp\left(\frac{(-h_i)}{H2}\right)\left[1-A*\tan^{-1}\left(\frac{h_i-hpbl}{B}\right)\right] \qquad h_b < h_i \le h_f, \tag{A.2}$$

$$N_0=\left(\frac{N_{PBL}}{\exp\left(\frac{-h_{PBL}}{H_2}\right)}\right). \tag{A.3}$$

For equation A.2 the leading variable A is solved at (N_{PBL}, h_{PBL}) by setting $N_2(h_i)=N(h_{PBL})$ and taking the derivative, such that $N_2'(h_i)=N'(h_{PBL})=\frac{dN}{dh}_{min}$. Isolate A to yield

$$A=-\left[\frac{\frac{dN}{dh}_{min}*B}{N_0 exp\left(\frac{-h_{PBL}}{H_2}\right)}\right]-\frac{B}{H_2}. \tag{A.4}$$

Return variable A to eq. A.2,

$$\frac{C_2}{B}=arctan\left(\frac{C_1}{B}\right). \tag{A.5}$$

Equation A.2 is evaluated at point (N_f, h_f) and arranged to isolate the arctangent function and leading coefficient A. The solution for A (eq. A.4) is then substituted into the equation. Variable B is factored out and both sides are divided by the remaining expression resulting in equation A.6. Both sides are then divided by B and the result is A.5.

$$C_2=\frac{\frac{N_f}{N_0 exp^{\left(\frac{-h_f}{H_2}\right)}}-1}{\frac{\frac{dN}{dh}_{min}}{N_0 exp^{\left(\frac{-h_{PBL}}{H_2}\right)}}+\frac{1}{H_2}}. \tag{A.6}$$

$$C_1=(h_f-h_{PBL}). \tag{A.7}$$

Equation A.5 is solved iteratively as the solution lies at the intersection of the expressions evaluated between $1e^{-6} \le B \le 1e^{6}$ with increment of $1e^{-6}$. The solution for A is the positive root solution for B.

Term three (N_3) uses the refractivity value at the top of the transition layer (N_f) and the scale height H_3 (A.15) is the statistical median of individual scale height profiles calculated from the MAGIC radiosondes,

$$N_3(h_i)=N_f*\exp\left(\frac{-(h_i-hf)}{H3\ (h_i)}\right) \qquad h_\mathrm{f} < h_i \leq h_{4\mathrm{bot}}. \tag{A.8}$$

The N_4 segment begins at point h_{4bot} (h=6.5 km), and the refractivity value equal to the point on the profile where N_{4bot} is explicitly set as the value of the N_3 segment at h=6.5 km. The top of the layer is h_{4top}=7 km and N_{4top}= 130.6 N-units.

$$N_4(h_i)=N_{4bot}*\exp\left(\frac{-(h_i-h4bot)}{H4}\right) \qquad h_{4bot} < h_i \leq\ h_{4\mathrm{top}}. \tag{A.9}$$

Segment (N_5) scale height value H_5 (A.17) is a statistical array.

$$N_5(h_i)=N_{4top}*\exp\left(\frac{-(h_i-h4top)}{H5\ (h_i)}\right) \qquad h_i > h_{4\mathrm{top}}, \tag{A.10}$$

For each MAGIC refractivity profile, a basic refractivity model (eq. A.11) is solved for the scale height value (H) from the surface (N_{sfc}, h_{sfc}) to the top of the profile (eq. A.12).

$$N(h_i)=N(h_\mathrm{sfc})*\exp\left(\frac{(-(h_i-h_{sfc}))}{H(h_i)}\right), \tag{A.11}$$

$$H(h_i) = \frac{-h_i - h_{sfc}}{\left((\ln N(h_i))-\left((\ln N\left(h_{sfc}\right))\right)\right)}. \tag{A.12}$$

Scale height values for each segment N_1 and N_2 are calculated by taking the median values between the layers specified in A.13 and A.14.

$$H_1 =< H(h_i) > \qquad h_1 < h_i < h_\mathrm{b}. \tag{A.13}$$

$$H_2 =< H(h_i) > \qquad h_\mathrm{b} < h_i < h_\mathrm{f}. \tag{A.14}$$

We assume the free-troposphere refractivity, i.e., N_3 segment (A.8) is an exponential decay with height above h_f, and can be rearranged for scale height H_3 such that,

$$H3\ (h_i) = \frac{-(h_i-h_f)}{\left((\ln N(h_i))-\left((\ln N\left(h_f\right))\right)\right)} \qquad h_\mathrm{f} \leq h_i < h_{4\mathrm{bot}}. \tag{A.15}$$

The scale height H_4 is between 6.5 km and 7.0 km and is calculated as a linear slope.

$$H_4=\frac{-\left(h_{4top}-h_{4bot}\right)}{\left(\ln N\left(h_{4top}\right)-\ln N\left(h_{4bot}\right)\right)} \qquad h_{4\mathrm{bot}} \leq h_i \leq h_{4\mathrm{top}}. \tag{A.16}$$

The H_5 segment is also a median array, similar to H_3.

$$H_5(h_i) = \frac{-(h_i-h_{4top})}{\left((\ln N(h_i))-\left((\ln\left(N_{4top}\right))\right)\right)} \qquad h_i \geq h_{4\mathrm{top}}. \tag{A.17}$$